ROYAL SOCIETY OF CHEMISTRY

REVIEW

Check for updates

Evolution of natural eyes and biomimetic imaging devices for effective image acquisition

Min Su Kim, †[ab] Ji-Eun Yeo, †[c] Hyeonseung Choi,[ab] Sehui Chang,[c] Dae-Hyeong Kim *[ab] and Young Min Song*[c]

In the natural evolutionary process, biological creatures have developed diverse visual structures apt for their habitational environments. These natural vision structures have inspired the development of artificial vision systems. These systems have numerous advantages in image acquisition compared to conventional imaging devices, including high visual acuity, motion sensitivity, simple accommodation, and low optical aberration. These advantages have contributed to the advances of various imaging devices for autonomous vehicles, mobile electronics, visual prostheses, and machine vision systems. Here, we reviewed recent advances in bio-inspired artificial vision systems that have mimicked the optical and retinal advantages of natural vision structures. These artificial vision systems have overcome many critical challenges in conventional image systems and presented potential for the next-generation image acquisition systems. The remaining challenges and the future outlook are also briefly described in the conclusion section.

1. Introduction

The eye is a vital organ for living creatures that can detect light and perceive visual information from their habitat. From the simple early eyes (*e.g.*, pigment pit and ocelli)[1–4] to highly advanced eyes (*e.g.*, chambered eye and compound eye), numerous creatures have optimized the function and structure of their eyes in response to different demands for their survival. Unlike the simple configurations in the early eyes that only sense ambient light levels,[5] advanced visual functions are essential for some creatures to cope with complex environments, such as determining the direction of light, distinguishing shapes and details, and discriminating colors.[6–10] For example, insects and crustaceans have evolved to have compound eyes composed of multiple ommatidia,[11–14] specialized for wide field-of-view (FoV) imaging and motion detection. They even can detect polarized light to figure out the moving direction. Birds and reptiles have evolved to have a unique structure called a fovea for high-resolution vision.[15–18] Some creatures have eyes that can detect ultraviolet (UV) or infrared (IR) light.[19–22]

These biological eyes have inspired us to develop imaging devices capable of acquiring visual information more efficiently. For example, imaging technologies have made steady progress by replicating the essential features of advanced vision systems in nature, including the iris (aperture), lens (artificial lens) and retina (photosensitive layer).[23–25] However, traditional imaging technologies still have significant scope for improvement in terms of simplicity, miniaturization, and other functional aspects.[26,27] For instance, digital cameras usually have flat photosensitive layers because they are manufactured on planar wafers through the conventional microfabrication processes. Field curvature is one of the frequently occurring optical aberrations in these flat image sensor systems, which refers to the deviation of the focal position from the basic curved image surface called the Petzval surface as the field angle increases.[28] The Petzval surface leads to bulk and complex lens configurations to focus the entire FoV onto the image plane of the flat imager.[29–31] If a curved type of image sensor is available, inspired by the curved retina in the biological chambered eyes, the number of lenses required for the imaging system to eliminate image distortion and aberration can be greatly reduced, and thus the system volume and weight can be significantly reduced.[32–35] Performance requirements for vision systems exhibit variability based on the operational setting and the intended application, thereby necessitating the consideration of distinct criteria such as resolution, FoV, and depth perception. Taking into account multiple crucial factors, the performance of recent artificial vision systems has been summarized and presented in Table 1.
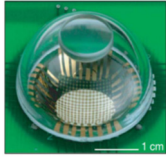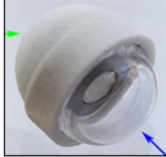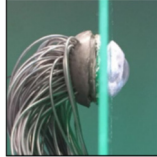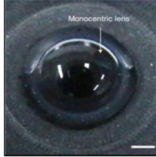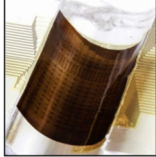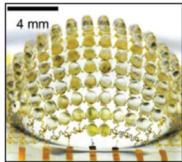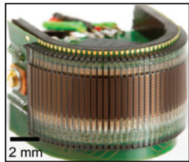
[a] *Center for Nanoparticle Research, Institute for Basic Science (IBS), Seoul 08826, Republic of Korea. E-mail: dkim98@snu.ac.kr*

[b] *School of Chemical and Biological Engineering, Institute of Chemical Processes, Seoul National University, Seoul 08826, Republic of Korea*

[c] *School of Electrical Engineering and Computer Science, Gwangju Institute of Science and Technology, 123 Cheomdangwagi-ro, Buk-gu, Gwangju 61005, Republic of Korea. E-mail: ymsong@gist.ac.kr*

† M. S. Kim and J.-E. Yeo contributed equally to this work.

Table 1 Performance parameters of artificial vision devices

Type of eye	Single-chambered eye				
Focal length	12 mm	100 mm	16 mm	d_{far} = 2.95 mm d_{5cm} = 3.90 mm	160.6 mm
Lens diameter	12 mm	6 mm	12 cm	4.1 mm	10 mm
Pixel size	$500 \times 500 \ \mu m^2$	$5.5 \times 5.5 \ \mu m^2$	1.6 mm (pitch)	$200 \times 125 \ \mu m^2$	$92.1 \times 93.8 \ \mu m^2$
# of pixel	256	2 033 600 (CMOS)	100	351	455
Field of view	$80°$	N/A	$150°$–$160°$	$120°$	$120° \times 70°$
Photograph					
Ref.	82	141	188	77	88

Type of eye	Compound eye				
Focal length	1.35 mm	550 μm	1.4 mm (total track length)	N/A	2 mm
Lens diameter	800 μm	172 μm	$\sim$100 μm	180 μm	40 μm
Pixel size	$160 \times 160 \ \mu m^2$	260 μm (pitch)	$1.75 \times 1.75 \ \mu m^2$	$1.25 \times 1.25 \ \mu m^2$	$210 \times 210 \ \mu m^2$
# of pixel	256	630	2 000 000 (CMOS)	18 100 000 (CMOS)	128
Field of view	$160°$	$180° \times 60°$	$68°$	$170°$	$300° \times 160°$
Photograph					
Ref.	85	86	110	81	172

Herein, we review recent advances in bio-inspired artificial vision systems, which aim for more efficient image acquisition than conventional image sensing devices. First, we briefly explain the evolutionary process that the natural vision systems have taken to understand the origin of the unique structures and functions of the biological eyes. Second, we introduce the structural and functional advantages of bioinspired devices in comparison to those of natural eyes. To mimic these distinct structural and functional features in the artificial vision system require advanced material strategies with novel fabrication/ design techniques, which are explained in each artificial vision system section. Finally, the current state of bio-inspired artificial vision devices and their future outlook are discussed.

2. Bio-inspired devices for efficient image acquisition

2.1. High-resolution vision

The evolution of visual systems began with simple non-directional photoreceptors, which have been then progressively developed into more complex structures for processing sophisticated visual tasks (Fig. 1a).[36] Non-directional photoreceptors are composed of one photoreceptor cell or several photoreceptor cells without additional optical structures, which can only conduct simple visual tasks from light intensity variations, such as changes in water depth, UV intensity, and shadow. Phototaxis animals have eye spots consisting of pigment cells and photoreceptor

cells, which can detect the direction of light through other structures (microvilli) that partially shade photoreceptor cells. These systems can also scan spatial information through body movements and detect subtle changes in light intensity. The typical low-resolution vision system consists of multiple photoreceptors within a pigment pit or cup to monitor various directions simultaneously. Photoreceptors in these systems have reduced acceptance angles, allowing sufficient spatial resolution to track objects or avoid collisions. Additionally, they can collect enough photons by stacking photoreceptor membranes with reduced acceptance angles.[37] The high-resolution vision has evolved to have a tiny acceptance angle of $\sim$1 degree for conducting complex visual tasks to detect prey and predators. As a result, focusing optics, such as lenses, have become essential elements during the evolution of high-resolution vision.

Single-chamber eyes and compound eyes are two representative types of high-resolution animal eyes (Fig. 1b). Both eyes have corneas and lenses that refract and focus light on photoreceptor cells. However, the anatomical structures of these two eye types are significantly different, resulting in different optical characteristics. The single-chambered eyes, found in vertebrates including human, consist of a single lens and a concave hemispherical retina with several millions of photoreceptor cells that enable high spatial resolution and high acuity. For example, the human eye has approximately 100 million rod cells and 6 million cone cells.[34] In particular, the unique retina structure, called fovea, allows high-acuity vision in a certain
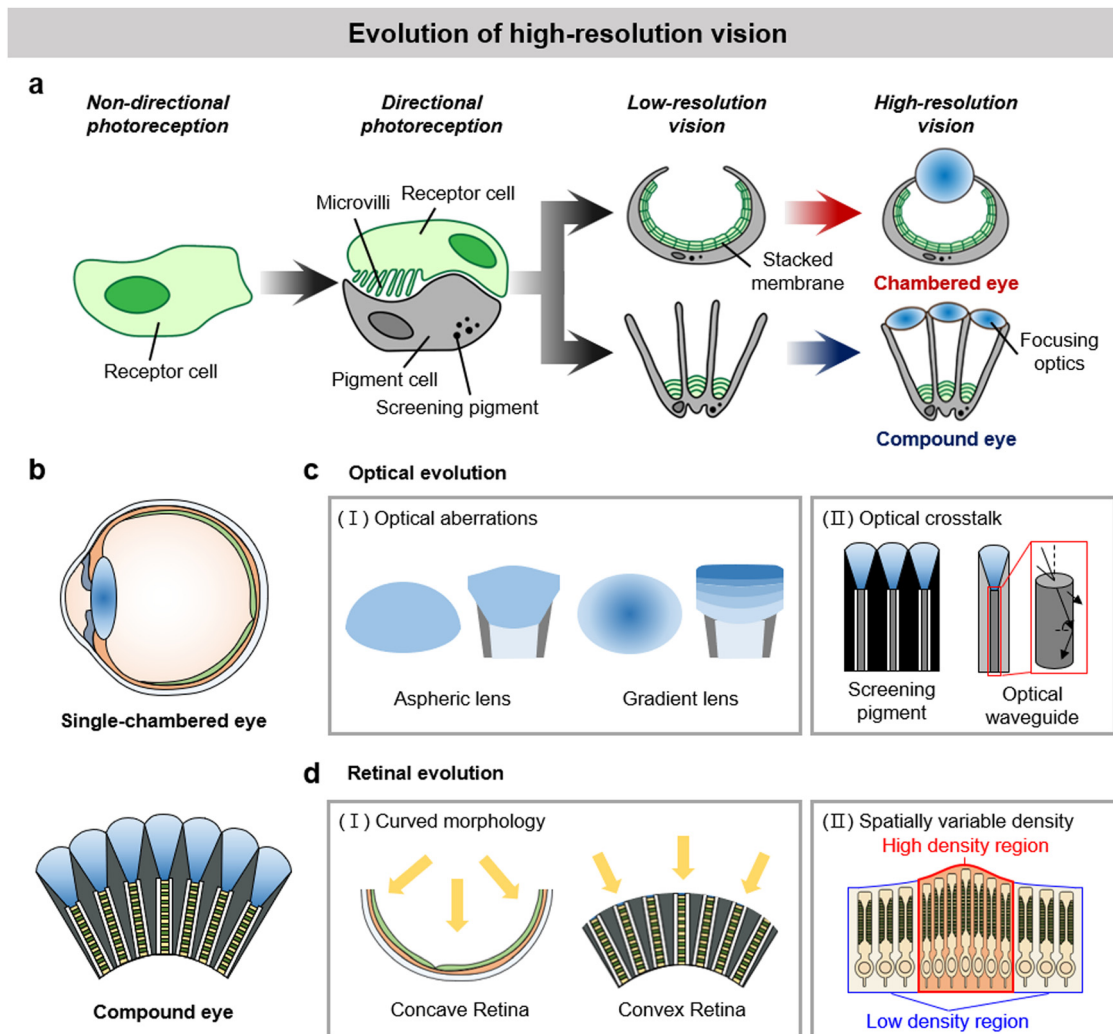
Fig. 1 Evolution of high-resolution vision. (a) Schematic illustrations of the evolution of visual system for sophisticated visual task. (b) Two representative types of the high resolution eye: single-chambered eye (top) and compound eye (bottom). (c) Evolution of optical structures for resolving issues that degrade the resolution, such as (I) optical aberrations and (II) optical crosstalk. (d) Evolution of the retina for the high-resolution vision, such as (I) curved morphology of retina and (II) spatially variable density of photoreceptor cells.

region of entire visual fields. On the other hand, the compound eyes, found in invertebrates such as insects and crustaceans, are composed of a convex-shaped array of thousands of unique optical units, called ommatidia. These eyes are specialized for wide FoV imaging due to the convex geometry and motion detection due to its high sensitivity.

Visual acuity, the ability to distinguish fine details, is determined by various factors, including anatomical features.[38] To achieve high acuity vision, densely packed photoreceptor cells in the retina and a long focal length are required. The inter-receptor angle is defined as a ratio of the distance between the receptors and the focal length so that the visual acuity is improved as the focal length increases.[39] In this regard, visual acuity is generally higher in large animals with large eyes because of the correlation between eye size and body size. Similarly, the compound eye has relatively lower acuity vision than the single-chambered eye of the same size because it has a small facet lens, which is particularly affected by diffraction.[26] For the compound

eye to achieve the visual acuity of human vision, it should be one meter in eye diameter.[13] In terms of the visual acuity range, animals with single-chambered eyes, such as humans, birds, mammals, and fish, typically have high visual acuity – for instance, ~ 60 cycles per degree (cpd) in human eyes,[38] bird eyes ranging from 4 to 140 cpd,[40,41] mammals from 0.1 to 64 cpd,[42,43] and fish eyes ranging from 0.56 to 40 cpd.[44,45] Insects and crustaceans with compound eyes show relatively low visual acuity, with maximum acuity of ~ 2 cpd.[11]

Other optical factors, such as spherical and chromatic aberration, also contribute to the resolution degradation. To circumvent these limits, animal eyes have evolved in diverse directions.[26] Some animals have evolved to correct the spherical aberration by adopting aspheric lens surfaces[46,47] and the chromatic aberration by using a crystalline lens with a gradient refractive index (GRIN) distribution[48–51] or a multilayered facet lens with graded indices[52,53] (Fig. 1c-I). Together with the diffraction and aberration in lens optics, the optical properties

of the retina are also important factors that determine spatial resolution. Optical crosstalk, which refers to the unintended light absorption by adjacent photoreceptors, can degrade spatial resolution.[39] To prevent resolution loss from the optical crosstalk, animal eyes, both single-chamber eye and compound eye, have evolved to confine light to the specific photoreceptor through additional structures such as screening pigments and optical waveguides (Fig. 1c-II).[11,54–56]

Achieving high visual resolution and acuity cannot be solely accomplished through lens optics alone or by preventing optical crosstalk. For example, conventional imaging devices often suffer from adjusting optical aberrations because a curved focal plane formed by a single lens does not match the flat image sensors.[57] Multiple lenses with complex lens optics (*e.g.*, the double Gauss lens) are required to address this issue, but it makes the imaging system heavy and bulky.[58,59] Moreover, the planar configuration of the conventional image sensor array has limited the implementation of the full panoramic FoV, which is a distinguished advantage of the natural compound eye.[60] Thus, the retinal evolutions found in natural eyes are necessary to be combined in artificial vision systems.

One of the most important features is the curved morphology of the retina (Fig. 1d-I). In the single-chambered eye, an object image focused by the single ellipsoidal lens creates a curved focal plane that matches the hemispherically curved concave retina. This allows high-resolution vision with a wide FoV and low optical aberrations while enabling a simple optical system configuration.[34,61] Meanwhile, hundreds of thousands of minimal sensing units called ommatidia contribute to imaging in the compound eye. Objects are focused onto a convex array of photoreceptors by individual facet lenses.[62,63] This configuration exhibits an infinite depth of field (DoF), wide FoV, and fast motion detection ability. Each ommatidium in the apposition compound eye consists of a facet lens, a crystalline cone, a light-guiding rhabdom, and photoreceptor cells.[26,64] Although the visual resolution of the compound eye is relatively inferior to the single-chambered eye, the apposition compound eye exhibits reasonable visual resolution *via* minimized optical aberrations, including distortion.[60]

Certain animals employ a spatially variable density of photoreceptors as an effective strategy to achieve high resolution (Fig. 1d-II).[65,66] By arranging a region of high-density photoreceptors in the central visual area and a relatively low-density region in the periphery, animals can achieve high visual resolution while minimizing redundant energy consumption.[67] For example, cuttlefish have a densely packed belt-like region in their retina that matches their main visual field.[68,69] Humans and birds also have a spot in their retina called the fovea, where cone cells are highly concentrated.[67] The fovea plays a crucial role by providing a clear and precise central vision, which is vital for tasks where the ability to distinguish fine details is of primary importance. It can be reading and driving for humans and hunting at a high altitude for birds.

As such, unique optical and retinal characteristics of the natural eyes have been developed through the long-term evolutionary process to achieve high resolution. Meanwhile, there have been continuous efforts to mimic such features found in natural visions and, thus, to develop highly efficient artificial vision systems. In this section, the detailed optical and retinal features, mimicked in artificial devices to achieve high resolution, will be reviewed.
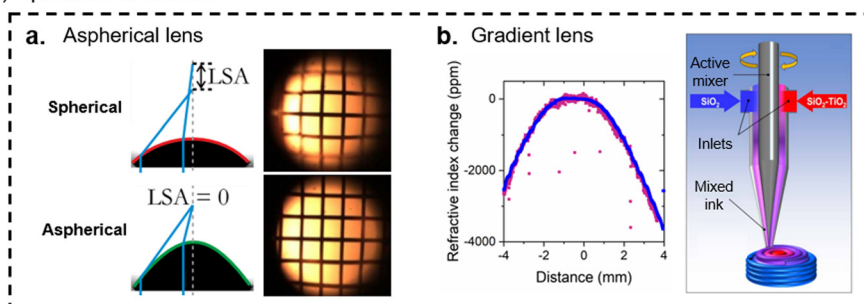
2.1.1. Optical evolution for high resolution vision. Over the past decades, inspired by animal eyes, extensive research works have been conducted to develop the artificial vision system (or artificial eye) from the development of optical parts to that of entire vision systems. For example, a tunable lens is demonstrated by applying electric fields on a liquid-based lens consisting of two liquids with different conductivities.[70–72] Mishra *et al.* suggested an aspherical liquid microlens to correct the spherical aberration by adjusting the interface shape between two non-mixable liquids, such as oil and water (Fig. 2a).[73] The lens system consists of three parallel glass plates held together by spacers, and the middle plate has a circular aperture with a 1 mm diameter. The lower space is filled with water, allowing for adjustment of hydrostatic pressure, while the upper space is filled with oil in the ambient pressure. When zero voltage is applied, the lens shows spherical curvatures that vary with the hydrostatic pressure, managing the longitudinal spherical aberration (LSA). By modulating the voltage (from 0 V to 3.3 kV) and the hydrostatic pressure (from 30 Pa to 88 Pa), the focal length and spherical aberrations can be controlled from 20 to 8 mm and from −1.79 to +1.13 mm, respectively.

Recently, various additive-based manufacturing methods have demonstrated significant potential in the fabrication of GRIN (Gradient-Index) lenses, one of which involves the sequential coating of layered polymer films.[74,75] However, there are several drawbacks associated with these methods, such as the requirement for precise control of the layer thickness and composition and the defect vulnerability because even a slight imperfection can substantially affect the lens quality. Rebecca *et al.* utilized a multi-material direct ink writing (DIW) approach to fabricate GRIN optical systems with customized refractive indices (Fig. 2b).[76] The DIW setup consisted of two inlets and a rotating active mixer inside the nozzle, and the desired concentration profile was achieved by controlling the concentrations of the two inks, silica (SiO_2) and silica–titania (SiO_2–TiO_2), in the mixer. Transparent SiO_2–TiO_2 GRIN glass, featuring an exponential index change of up to 0.008 and a transmittance exceeding 74%, was printed over a range of 1 cm by using the spatial variation in TiO_2 concentration to create a GRIN profile. Although the fabricated lens is shaped to a simple cylindrical form, the DIW is one of the promising methods for precise control of the optical or other material properties for gradient optics.

In another example, Kim *et al.* reported a miniaturized artificial eye camera inspired by the optical advantages of aquatic animals, including wide FoV and high visual acuity, by implementing the multi-focal lens (Fig. 2c).[77] To minimize the chromatic aberrations of monocentric lenses, a core–shell structure with two different RI values were fabricated by assembling two half-ball lenses, composed of a half-ball lens (BK7) and a shell lens (SF16), on both sides of the aperture using transparent
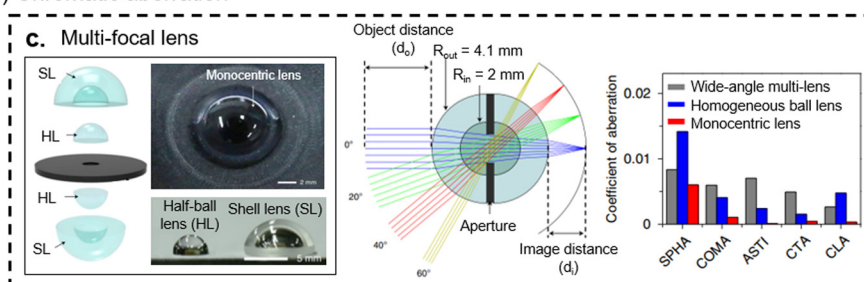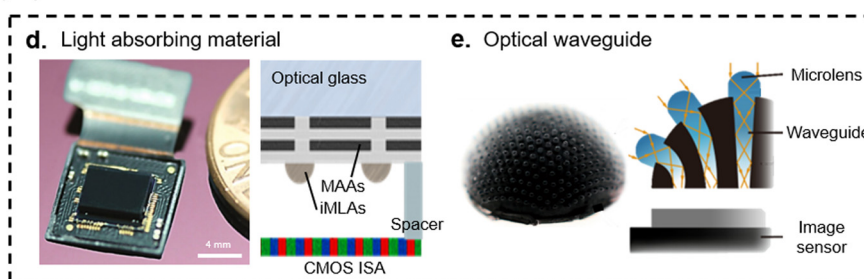
Fig. 2 Artificial vision systems that mimic the high-resolution capabilities of natural eyes using optical evolutionary methods. (a) Interface profiles of a spherical lens at zero voltage (top) and of an aspherical lens with zero spherical aberration when the voltage is applied (bottom) with optical images of a square grid demonstrating the correction of aberrations. Reproduced with permission.[73] Copyright 2014, Scientific Reports. (b) Spatial variation in the refractive index of the gradient refractive index (GRIN) glass optics (left) and fabrication method of the GRIN optical system from two silica-based inks with different dopant concentrations (right). Reproduced with permission.[76] Copyright 2020, Science Advances. (c) Exploded schematics and photographs of the multi-focal lens inspired by aquatic animals (left). Ray-tracing simulation (middle) and Seidel aberration coefficients (right) show significant reduction of chromatic aberrations in the multi-focal lens system. Reproduced with permission.[77] Copyright 2020, Nature Electronics. (d) Photograph (left) and cross-sectional image (right) of an ultra-thin arrayed camera inspired by the light absorbing materials in the Xenos-peckii vision system. Reproduced with permission.[80] Copyright 2020, Light: Science & Applications. (e) Photograph (left) and cross-sectional image (right) of a biomimetic vision system inspired by the optical waveguide of the natural apposition compound eye. Reproduced with permission.[81] Copyright 2021, Nature Communications.

optical adhesives (NOA61). Compared to a homogeneous ball lens, the utilization of different refractive index (RI) dispersion in GRIN lenses resulted in a notable reduction in overall chromatic aberrations, including chromatic transverse aberration (CTA) and chromatic longitudinal aberration (CLA). Specifically, the CTA was reduced from 1.51×10^{-3} to 4.30×10^{-4}, and the CLA was reduced from 4.77×10^{-3} to 3.14×10^{-4}.

Compared to the single-chambered eye, the compound eye has several unique features, such as smaller size, wider FoV, and improved sensitivity to motion. With these optical advantages, several artificial compound eye systems have been

demonstrated.[33,78,79] Kim *et al.* reported ultra-thin arrayed cameras for high contrast and high-resolution imaging with minimal optical crosstalk, inspired by the compound eye of Xenos-peckii (Fig. 2d).[80] Natural eyes improve the resolution by reducing optical crosstalk through pigment cells. Xenos-peckii's eyes contain pigment cups surrounding each eyelet to block incident off-axis light. The proposed system consists of a multi-layer aperture array (MAA), an inverted microlens array (iMLA), and a gap spacer on a planar CMOS image sensor array (CMOS ISA). With the stack of the black polymer (GMC 1040) with a circular pattern, MAA acts as a cylindrical pinhole array,

which absorbs light and reduces optical crosstalk between microlenses, which enables high contrast and high-resolution imaging.

Bo *et al.* utilized 3D printing methods with microfluidic-assisted molding to develop a biomimetic apposition compound eye (BAC-eye) (Fig. 2e).[81] The BAC-eye consists of 522 microlenses, with each microlens optically connected to the flat bottom of the hemisphere by a waveguide. The hemispherical element consists of a photosensitive polymer dyed with a black dye to absorb the scattered light, and the waveguide consists of room-temperature-vulcanizing (RTV) silicon that is optically transparent in the range of 400–1100 nm. The proposed system not only imitates the natural compound eye in terms of its small form factor and wide FoV but also delivers light from the microlenses arranged along the hemispherical surface to its flat base.

2.1.2. Retinal evolution for high resolution vision. Because most of the silicon processing method is limited to the planar device, conventional image-sensing devices based on flat substrates cannot be free from optical aberrations. To overcome this limitation, Ko *et al.* reported a novel method to implement curvature in the silicon image sensor array (Fig. 3a, left).[82] The method was used to fabricate an electronic eye (e-eye) camera with a 16×16 hemispherical curved pixel array. To fabricate
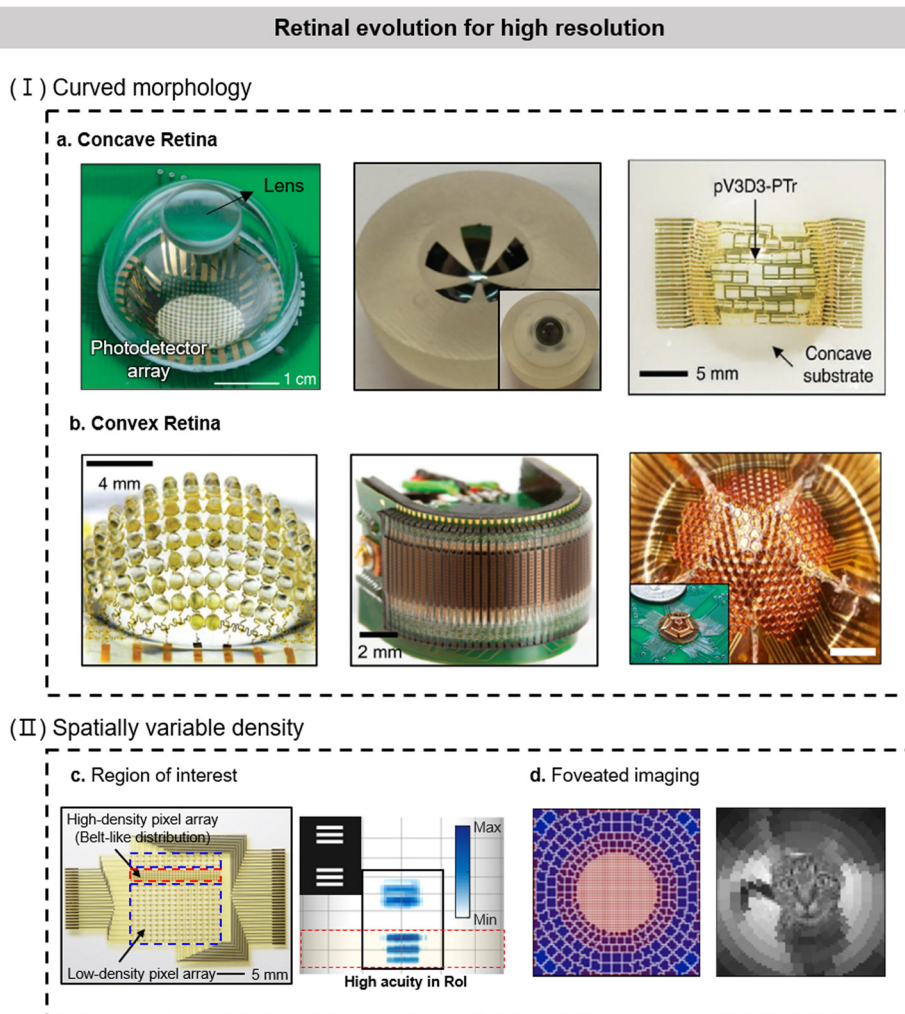

Fig. 3 Artificial vision systems that mimic the high-resolution capabilities of natural eyes. (a) Artificial vision systems inspired by the concave retina of single-chambered eyes. A hemispherical camera using a flexible silicon photodetector array and a single lens (left). Reproduced with permission.[82] Copyright 2008, Nature. Curved image sensor based on a tessellated hexagon structure. The inset shows the integrated monocentric imager with a single spherical lens (middle). Reproduced with permission.[32] Copyright 2016, Microsystems & Nanoengineering. Curved neuromorphic image sensor using a MoS$_2$-pV3D3 phototransistor array (right). Reproduced with permission.[58] Copyright 2020, Nature Communication. (b) Artificial vision systems inspired by the convex retina of compound eyes. Digital camera inspired by the compound eye of arthropod (left). Reproduced with permission.[85] Copyright 2013, Nature. Miniaturized (middle) and origami-structured (right) artificial compound eyes. Reproduced with permission.[86,87] Copyright 2013, PANS and 2017, Nature Communication. (c) Photodiode array that has spatially variable pixel distribution (left). The imaging demonstration shows a high acuity image in the high-pixel density region that matches with the region of interest (RoI) (right). Reproduced with permission.[88] Copyright 2023, Science Robotics. (d) Spatially variant pixel grid containing 1024 pixels (left) and reconstructed image of a cat (right). Reproduced with permission.[89] Copyright 2017, Science Advances.

the camera, a liquid prepolymer of polydimethylsiloxane (PDMS) was poured and cured between two hemispherical molds. After removing the molds, the PDMS was radially stretched, and a silicon photodetector array connected with compressible metal interconnections was transferred onto the PDMS. When the tensile strain was released, it deformed into a hemispherical shape. Finally, the array was transferred to a hemispherical glass substrate to integrate the optics and interconnections. This imaging system provides several advantages compared to the planar imaging system, including uniform focus, minimal distortion across the entire image plane, and a wide FoV.

As another alternative to conventional designs, Wu *et al.* made a hemispherical imaging device by assembling flexible gore segments composed of tessellated hexagonal photodiodes (Fig. 3a, middle).[32] A silicon-on-insulator (SOI) wafer with a 20 μm-thickness-device layer was used for the photodiodes, and the device layer was released by XeF_2 dry etching after all device fabrication processes ended. Each hexagonal photodiode was connected by spring-like bridges, functioning as deformable electrical connections. These bridges provide mechanical flexibility between semi-rigid hexagonal cells. Because the device has a unique hexagonal shape, the polar coordinate system was applied to address the individual cells, rather than conventional row-column addressing structure. The mechanical strength of the device was improved by coating it with the Perylene-C film, allowing it to be conformally transferred onto a hemispherical device holder. A high-performance monocentric imager was created by combining the device with a single spherical lens, resulting in a wide (160°) FoV.

Studies were also conducted on producing curved imaging devices using commercial CMOS image sensors. Guenter *et al.* used a pneumatic forming process to impart curvature to the commercial CMOS image sensor.[83] In the traditional method of forming curved membranes, the edges of the membrane are fixed while pressure or vacuum is applied, resulting in deformation resisted by increasing nonlinear radial tensile stress. In contrast, the pneumatic forming process introduces a flexible membrane under pressure that allows the die to move freely at the edges. A thinned and released die was placed into a forming mold and pneumatic pressure was applied to a compliant polymer membrane. As the pressure increased, the membrane gradually deforms and contacts the die from the corners inward. Using the method, commercial silicon CMOS image sensors can be thinned and formed into curved optical surfaces without functional degradation. As a result, it can effectively reduce radial tensile forces and minimize strain energy density while achieving an 18.74 mm radius of curvature. The curved sensor was then combined with custom lenses in a prototype camera, which exhibited a resolution of 3220 line-widths per picture height at an aperture of f/1.2 and nearly 100% relative illumination across the field. Similarly, Itonaga *et al.* fabricated an imaging system that composed of hemispherically curved CMOS image sensor and integrated lens.[84] After fabricating the ordinary CMOS image sensor on a planar silicon wafer, tensile stress was applied throughout the sensor region to deform it into curved shape. In the image circle, the sensitivity of system increased at the

center by 1.4 times and doubled at the edges. The dark current was also one-fifth lower than that of the planar device.

Although these e-eye cameras possess aberration-free characteristics and feature a simple device structure, they cannot implement efficient data processing like human neural network. To solve this problem, Choi *et al.* proposed a curved neuromorphic imaging device inspired by human vision (visual data acquisition and recognition) system (Fig. 3a, right).[58] A heterostructure of MoS_2 and pV3D3 on a Si_3N_4 substrate was integrated with graphene source/drain electrodes to fabricate a phototransistor array. The time-dependent photo-responses of MoS_2 and pV3D3 phototransistors realized a high-quality short-term plasticity and a long-term potentiation, similar to the mechanism of the human image recognition system. Due to the ultrathin and intrinsically flexible materials used to fabricate the device, including thin active materials (graphene, MoS_2 and pV3D3), encapsulation (polyimide) and metal interconnections (Au and Cr), it was able to be transferred onto the hemispherically curved concave PDMS mold without malfunction. Based on this characteristic, the curved neuromorphic image sensor array can achieve high efficiency in acquiring images and pre-processing the acquired image data.

Among the hemispherical designs, the aforementioned concave-shape photodiode array represents the artificial version of the retina of vertebrates. Meanwhile, the double-eyed structure of arthropods is represented by the convex form of the artificial retina. Since each type has its advantage, the convex-type e-eye cameras have also been steadily developed. For example, Song *et al.* presented a hemispherical bio-mimetic e-eye camera inspired by the arthropod eye (Fig. 3b, left).[85] The device has a convex surface consisting of a hemispherical PDMS mold with 16×16 microlenses and thin silicon photodiodes. First, the photodiode array and PDMS microlenses array were aligned and integrated on a planar substrate. After combining them, stress was applied to transform the planar device into a hemispherical convex structure. A narrow filamentary serpentine-shaped design was developed to minimize stress on the interconnections, incorporating Cr/Au materials and polyimide encapsulation. The device can obtain signal from each pixel, and imaging was performed by synthesizing and processing the signal obtained from each activated photodiode. Additional imaging processes for various angles (left: −50°, centre: 0°, and right: 50°) and distances (12 mm, 22 mm, and 32 mm) were also performed. The result was nearly distortion-free, and the FoV of ∼160° was obtained. Even though the object distance increased, there was no change in the focus, showing an excellent DoF.

Floreano *et al.* proposed another unique structure for the bio-inspired compound eyes (Fig. 3b, middle).[86] The device consists of three planar layers, and each layer was bent to implement the convex structure. The first layer is a transparent polymer microlenses array, the second layer is a photodetector array with a processing circuit, and the last layer is a polyimide printed circuit board (PCB) which is used as a flexible interconnection and support substrate. The upper two layers are based on a planar fabrication and have 42 columns of 15 imaging elements. These layers are too rigid to be bent to a convex

structure, so each chip was diced to be easily deformed. As an interconnection layer and supporting substrate, a flexible PCB connects each pixel and is bent to implement a curved structure. To get a horizontal FoV of 180°, the angle between each pixel is set at ~4.3°. Although there is no vertical bending on the device, through the stepwise gap between the lens and the photodetector, a FoV of ~60° was constructed. Also, the photodetector layer has a neuromorphic adaption circuit to solve the nonresponsive problem of the saturated photoreceptor. The application of neuromorphic circuits, which mimic the local adaptation of light in animals, reduces the dullness of illumination changes due to photoreceptor saturation and enables faster reactions. This biomimetic compound eye is expected to be used in various fields related to motion detection with high temporal resolution and local light adaptations.

Zhang *et al.* presented an origami structure to transform the planar structure into the ideal aberration-free concavely hemispherical structure (Fig. 3b, right).[87] Using the truncated icosahedron structure, the planar film can be transformed into a soccer ball-like hemispherical structure when the origami structure is folded. The device can be transformed into either a concave or convex shape. The convex structural focal plane array (FPA) is suitable for arthropod-inspired e-eyes, while the concave structural FPA is highly related to the eye of vertebrates. When a laser was radiated onto the convex hemispherical array, the imaging result showed a blurred image (blurring can be explained by the lack of additional elements optimizing the image). However, the key advantage of this approach is the possibility of implementing a two-way hemispherical structure with a simple structure at a low cost. Also, various isolating elements or image processing methods can solve the blurring issue.

Golden cuttlefish (Sepia esculenta) has a densely packed area of photoreceptors in their retina, forming a belt-like structure slightly above the equator. This particular region of the retina enables the cuttlefish to have excellent visual acuity within its region of interest (ROI), which is optimized for detecting moving objects near the horizon. Like the cuttlefish eye, Kim *et al.* designed a photodiode array with a belt-like high-density area and a peripheral low-density area (Fig. 3c).[88] The photodiode array is then transferred onto a concave cylindrical PDMS mold and integrated with an artificial lens and aperture to fabricate the imaging device. The lens used in the device has a negative magnification, which forms an inverted image on the photodiode. Thus, the high-density pixel region located above the center line can produce a highly detailed image of the lower visual field below the center line of the horizon. In order to verify the ability of the high-pixel density region to capture high-acuity images in the ROI, line pair objects were placed either above or below the center-line. The high-pixel density region produced a clear image of the line pair objects in the lower visual field, while the low-pixel density region produced a blurry image of the line pair objects in the upper visual field.

Compared to the conventional multi-pixel imaging method, the single-pixel imaging method relies on measuring the correlation between the scene and a series of patterns. However, capturing a complete scene using single-pixel systems usually suffer from low frame rates, because the least number of correlation measurements has to be the same as the number of pixels in the reconstructed image. To address this issue, Phillips *et al.* enhanced the data gathering capacity of the single-pixel imaging system by using adaptive foveated imaging (Fig. 3d).[89] The number of pixels in each raw frame was decreased and the frame rate was increased through radial pixel size variation. As a result, smaller pixels are distributed in the central high-resolution foveal region while larger pixels are distributed in the surrounding areas. Imaging with the uniform and spatially-variant resolution was conducted with the 32 × 32 pixel grid with a total of 1024 pixels. Both images required the same measurement resources, but the nonuniform foveated image had twice higher linear resolution in the central region, enhancing the details of the image while reducing the resolution in the surrounding areas.

2.2. High sensitivity vision

High sensitivity is one of the key features in the biological vision, although an inherent trade-off exists between resolution and sensitivity in all eye designs. Eye sensitivity refers to the ability to capture photons and quantify the number of photons captured per receptor, which is a critical factor for nocturnal animals and deep-sea animals living in dim environments. As one of the simplest solutions to improve visual sensitivity, animals have been selected to have a low F-number, defined as a ratio of focal length to the diameter of the pupil or aperture (Fig. 4a-I).[39,90] The accumulated data of the F-numbers in nocturnal and diurnal species revealed that the former generally exhibit relatively low F-numbers between 0.5 and 0.9, whereas the latter have F-numbers greater than 1.3.[91] In addition, the shape of the pupil affects the light collection, particularly concerning the habitat and lifestyle of the species. For instance, some cephalopods, such as cuttlefish and squid, have a peculiar pupil of a w-shape or u-shape, which is specialized to reduce intense light incidents from the upper side.[92,93]

The mechanism of enhancing sensitivity is not limited to single-chambered eyes; it is also frequently observed in compound eyes. The apposition-type compound eyes have difficulty in collecting enough photons under dim environments. On the other hand, the nocturnal or deep-sea compound eyes have evolved into superposition-type eyes to increase visual sensitivity by capturing photons incident from adjacent ommatidia rather than blocking them to prevent the optical crosstalk (Fig. 4a-II).[12,26] Nocturnal moths have adapted to dim light environments by developing unique nanometer-scale structures with subwavelength scale periods on their ommatidium, called anti-reflective (AR) structures (Fig. 4a-III).[94-96] These nanostructures are composed of tiny ridges smaller than the wavelength of light, which induces the effective RI to change gradually between the air and the eye. In this way, incident light does not undergo a rapid change in the RI, effectively reducing the amount of light reflected from the surface of the eye. This structure increases sensitivity in dim light environments and reduces eye-glow
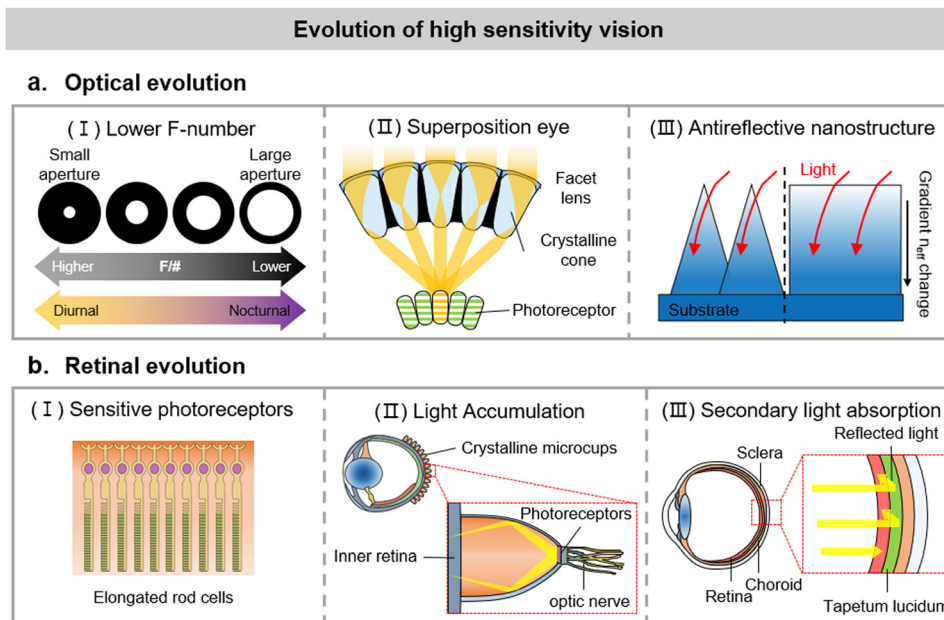
Fig. 4 Evolution of high-sensitivity vision. (a) Evolution of optical structures for high-sensitivity vision, such as (I) lower F-number, (II) superposition eye, and (III) Antireflective nanostructure. (b) Retinal evolution for high-sensitivity vision such as (I) sensitive photoreceptors, (II) light accumulation, and (III) secondary light absorption.

phenomena that predators can see, making it more difficult for them to detect the moths.[26]

Another option to enhance light sensitivity is to improve the light absorption capability of photoreceptor cells.[26,97,98] One approach is to increase the light path that the light takes within the photoreceptor.[99] This allows incident light to have a higher probability of absorption. Cichlid possesses elongated rod cells that exploit this mechanism to achieve high light sensitivity (Fig. 4b-I).[100] Additional optical structures have been used to improve light absorption, such as light accumulating structures in front of the photoreceptors (Fig. 4b-II) or rear light reflectors that provide secondary light absorption (Fig. 4b-III). A representative light-accumulating structure appears in elephant nose fish with crystalline microcups with reflecting photonic crystal sidewalls in the retina.[101] The cone photoreceptors are grouped within reflecting, photonic crystalline cups, receiving guided light rays through an enclosed structure. For the biological light reflector, tapetum lucidum is the representative structure that some nocturnal and deep-sea animals have behind their retina.[102–105] It reflects visible light back through the retina, increasing the light amount available for the photoreceptors to absorb.[106] Especially for the cat, the tapetum lucidum increases vision sensitivity by 44%, allowing the cat to see the imperceptible light to human eyes.[107] In this chapter, we discussed the optical and retinal evolution of high-sensitivity natural visions and the corresponding development of high-sensitivity artificial vision systems.

2.2.1. Optical evolution for high sensitivity vision. In low-light conditions, the human iris undergoes a process called pupillary dilation, whereby the central aperture of the iris expands, allowing more light to enter the eye and reach the optic nerve.[31] In order to improve light sensitivity inspired by the human iris, Kim *et al.* developed an iris-like actuator using a graphene-oxide-loaded crosslinked PNIPAm (PNIPAm/GO) hydrogel (Fig. 5a).[108] The hydrogel exhibits significant volume variation, which enables the actuator to function similarly to the human iris. When the hemispherical hydrogel iris is exposed to light, the size of the internal hole decreases, reducing the amount of light heading to the photodiode; however, when the light is turned off, the photocurrent increases according to the increased amount of light due to the volume recovery of PNIPAm/GO. In addition, the PNIPAm/GO hydrogel can also be adjusted by temperature and electricity.

The superposition eye can be further classified into four types according to the structures and functions: refractive superposition type, reflecting superposition type, parabolic superposition type, and neural superposition type.[78,109] Inspired by the neural superposition type compound eye, Keum *et al.* reported ultra-thin digital cameras with improved sensitivity and spatial resolution (Fig. 5b).[110] The camera comprises two stacks of curved microprism arrays and planar microlens arrays integrated into a conventional CMOS image sensor (CIS). The camera has a diameter of 3.4 mm and a thickness of 1.4 mm, offering a FoV of 68 degrees. In order to enhance the final image resolution, the array of images obtained from microlenses are combined to reconstruct a single high-resolution image.

Several light field camera systems have been reported as one of the neural superposition-type compound eye applications. The light field camera (LFC) is an imaging device that can extract depth data of objects by using light-field information. Compared to traditional cameras, LFCs are able to conduct functionalized imaging techniques such as depth estimation
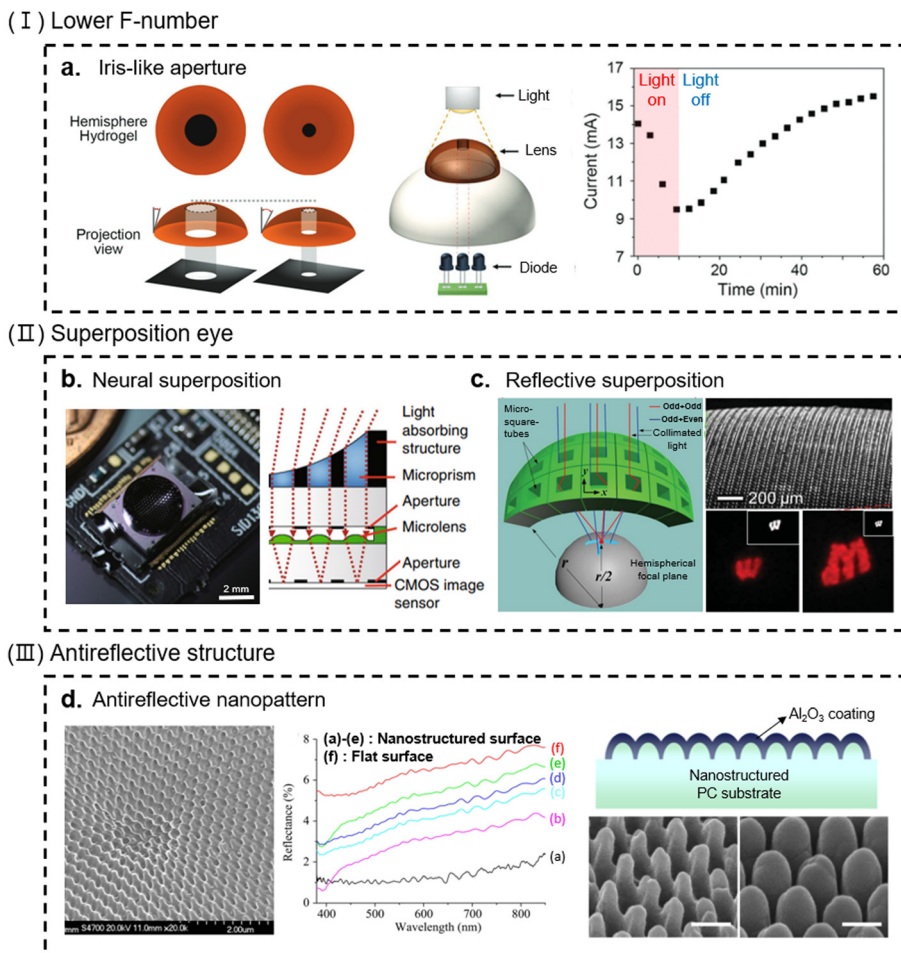
Fig. 5 Artificial vision systems that mimic the natural eyes with high-sensitivity imaging capabilities resulted from evolution of unique optical structures. (a) Comparison for the shape of the actuator between low-light and bright-light conditions (left) and experimental setup for determining light transmittance (middle) inspired by the low F-number of natural eyes. Photocurrent increases when no light projection (right). Reproduced with permission.[108] Copyright 2019, Macromolecular Materials and Engineering. (b) Photograph (left) and cross-sectional image (right) of an ultra-thin digital camera inspired by the neural superposition type compound eye. Reproduced with permission.[110] Copyright 2018, Light: Science & Applications. (c) Exploded schematic of the artificial vision system inspired by reflective superposition compound eyes (RSCEs) (left) and SEM image of reflective micro-square tube array (right, top). Image characteristics comparison between commercial refractive lens (right, lower left) and artificial RSCEs (right, lower right). Reproduced with permission.[120] Copyright 2014, Small. (d) SEM image of PDMS female mold (left) and reflectance spectra of antireflective (AR) nanostructure (middle). Curves (a)–(e) represent nanostructure surfaces according to different imprinting forces and curve (f) represents the fat PC substrate. Reproduced with permission.[130] Copyright 2018, Scientific Reports. Cross-sectional image of AR nanostructure (right, top). SEM image of before (right, lower right) and after (right, lower left) atomic layer deposition (ALD). Reproduced with permission.[131] Copyright 2019, Optical Materials Express.

and focal depth expansion.[111–114] Inspired by the optical structure of trilobite, one of the earliest arthropods with compound eyes, bioinspired LFCs that can store DoF and achieve high-resolution light field imaging are also implemented.[115] LFC technology is being applied in a variety of new applications, along with technological improvements such as the high resolution image sensors and miniaturization of the imaging system.[116–119]

To mimic a reflecting superposition-type eye, Huang *et al.* integrated an elastomeric polymer and a micro-square tube array surrounding four highly reflective sidewalls to improve light sensitivity. (Fig. 5c).[120] Due to the convex shape and

Al-coated reflecting plate, the incident light is reflected by the sidewalls and then focused onto a single photodetector in a superimposed way of overlapping the light from multiple micro-square tubes, so that the light sensitivity of the device increases. This 3-dimensional, hemispherical artificial reflecting superposition-type compound eye can achieve wide FoV, low aberration, and enhanced sensitivity to light.

Moth eyes have inspired the development of a technique for reducing the reflection of incident light by using gradient index coatings with highly ordered structures. To implement the structure, many surface treatment methods have been suggested.[121–123] Nanoimprint lithography (NIL) is one of the

representative AR technologies that offers several advantages, such as high precision, high efficiency, simplicity of operation, and low cost.[124–129] Sun *et al.* reported the fabrication of AR structures on the surface of a transparent polycarbonate (PC) substrate using the Roll-to-Plate (R2P) UV-NIL method (Fig. 5d, left and middle).[130] The R2P UV-NIL method involves a pattern imprinting onto a flexible substrate using a roller mold and UV-curable resin. In this study, the reflectance of the AR sub-wavelength structure (SWS) was investigated as a function of the height of the periodic structure. The reflectance decreased as the height of the AR SWS increased. The average reflectance of the AR SWS sample was only 1.21% in the visible light range at normal incidence.

Meanwhile, since the nanostructures are vulnerable to mechanical deformations such as pressure and scratches, the way to improve the durability of AR SWS has been investigated. Yoo *et al.* reported an AR moth-eye structure with an oxide coating to enhance the surface hardness (Fig. 5d, right).[131] The AR SWS has a period of 250 nm, a height of 300 nm, and a filling fraction of 75%. The atomic layer deposition (ALD) has been used to deposit a uniform aluminum oxide (Al_2O_3) mono-layer of various thicknesses onto the surface of AR SWSs. The scratch resistance of AR SWSs was measured using a nano-scratch resistance measurement technique with a diamond stylus. The average friction coefficient was reduced by approximately 20% in samples coated with a 100 nm thick layer of Al_2O_3, compared to the uncoated samples. This indicates that the thickness increase in the Al_2O_3 coating is effective in scratch resistance. The AR nanostructures have been widely adopted in various applications, such as solar cells and photo-detectors, to increase device efficiency.[132–138]

2.2.2. Retinal evolution for high sensitivity vision. Incident light gets a greater chance to be absorbed within the elongated rod cells of the cichlid, owing to the longer path that the light takes. Thus, cichlid shows high light sensitivity even in a dim underwater environment. Such a mechanism inspired Kim *et al.* to use nanorod texturing to enhance the photo-absorption and light sensitivity of the silicon photodiode (Fig. 6a).[77] Based on the wave optics to reduce surface reflection and transmission, the silicon nanorods (SiNRs) were designed to have a height of 220 nm, diameter of 200 nm and pitch of 520 nm. Compared to bare silicon, the SiNRs exhibited improved photo-absorption in the visible spectrum. This enhancement can be attributed to the light trapping effect caused by the diffraction at the nanorod structure and elongated light path for photo-absorption.[99] However, due to the creation of dangling bonds that generates surface leakage current, nanorod texturing of the silicon surface increases the dark current (I_{dark}).[139] Also, the presence of surface dangling bonds creates charge carrier recombination sites, which lead to a decrease in the photocurrent (I_{photo}).[99] To solve the problem, Al_2O_3 was deposited on the SiNRs to passivate the surface. The dangling bonds can be removed by surface passivation, preventing surface leakage current and charge carrier recombination.[139,140] As a result, the dark current decreases and the photocurrent increases, significantly increasing photosensitivity (I_{photo}/I_{dark}).

Liu *et al.* enhanced the incident light intensity by collecting the light through artificial microcup reflectors (Fig. 6b).[141] The idea comes from the retinal structure that elephantnose fish (Gnathonemus petersii) have developed. Each microcup is based on a laser-patterned glass microstructure with two opposite facets and four parabolic sidewalls. SU-8 photoresist was sprayed on the sidewalls to smooth the surface and reduce the scattering losses. Then, the aluminum layer ($\sim$150 nm) was sputtered onto the sidewalls to concentrate the incident light from the large facet (input port) to the small facet (output port). When the height and input-port diameter of a microcup was fixed at 120 μm and 77 μm, the microcups with an output-port diameter of 20 μm produced the greatest enhancement in light intensity. Unlike its natural counterpart, which reflects only red light, the microcup reflectors possess a wide-spectrum optical property that makes them compatible with most artificial image sensors. This improves the light intensity by more than three times over the entire visible light spectrum (wavelength from 400 to 780 nm). For the imaging demonstration, an optical setup with a flat 48 × 48 microcup array and a mono-chrome charge-coupled device (CCD) was constructed. The target object without a reflector was difficult to identify under a low-light conditions (where the light intensity is 0.05 μW cm^{-2}), whereas the target object with reflectors produced much brighter and more recognizable images. An artificial eye was also fabricated by integrating an artificial cornea, ball lens, iris and microcup array supported by a hemispherical PDMS membrane. However, image distortion occurred due to the mismatch between the curved image plane and the flat image device, which remains to be improved.

Min *et al.* fabricated a deformable inverse opal structure based on silk hydrogel (Fig. 6c).[142] To prepare the silk hydrogel inverse opal (SHIO), first, poly(methyl methacrylate) (PMMA) nanospheres with a diameter of 300 nm were deposited into a face-centered cubic (fcc) structure on a silicon substrate. After the PMMA template was filled with a mixture of silk fibroin and stilbene solution, the solution was cross-linked by exposing it to short-wavelength UV light. Finally, the silk-PMMA composite was detached from the substrate and immersed in acetone to dissolve the PMMA, generating an inverse opal structure. Due to the deformability of the SHIO, it can be conformally mounted on the hemispherical agarose gel. When a red laser beam illuminated the SHIO, scattered light was partially concentrated at the interface between the SHIO and agarose gel, while some of the light was reflected back to the opposite direction. Optical simulation using the finite-difference time-domain (FDTD) method confirmed that the reflected beam was focused precisely at the focal point, indicating the functionality of the SHIO as a concave reflector. Both concentrated and reflected light can be attributed to the light absorption enhance-ment of photoreceptors in front of the SHIO. Additional measure-ment with blue dye (gardenia blue) solution, which absorbs a broad-band spectrum ranging from green to red light, was con-ducted to verify the phenomenon. Compared to the measurement without SHIO, the measurement with SHIO showed improved absorbance of white light in the broad range of 510–660 nm.
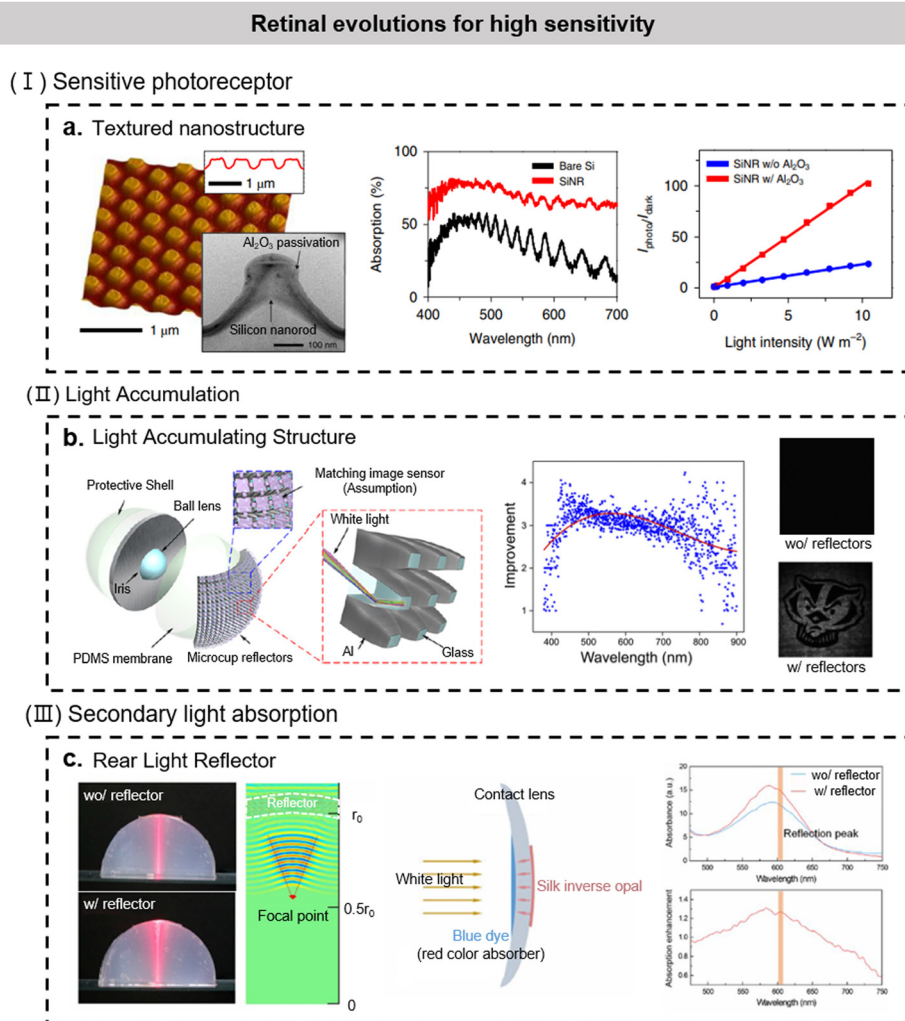
Fig. 6 Artificial vision systems that mimic the natural eyes with high-sensitivity capabilities resulted from evolution of unique retinal structure. (a) Three-dimensional atomic force microscopy (AFM) image showing surface morphology of silicon nanorods (SiNRs). Inset shows the cross-sectional TEM image of SiNRs (left). Comparison for the absorption characteristics of bare silicon and SiNRs in the visible spectral range (middle). Sensitivity (I_{photo}/I_{dark}) of SiNR photodiode with and without Al_2O_3 passivation measured at different light intensities (right). Reproduced with permission.[77] Copyright 2020, Nature Electronics. (b) Exploded schematic of the artificial vision system inspired by the retinal structure of elephantnose fish (left). Enhancement of light intensity (blue dots) and cubic polynomial fit of the data (red line) at wavelength ranging from 380 to 900 nm (middle). Imaging demonstration under low light condition (0.05 $\mu W\ cm^{-2}$) showing enhanced imaging quality with microcup reflectors (right bottom). Imaging without microcup reflectors cannot recognize target object (right top). Reproduced with permission.[141] Copyright 2016, PNAS c) Photographs of the reflection behavior of a red laser beam with and without inverse opal reflector. The FDTD simulation proves that the reflector serves as a concave mirror (left). Schematic illustration of experimental setup (middle) and measurement (right) to verify the absorption enhancement. Reproduced with permission.[142] Copyright 2017, PNAS.

The simulation and measurement proved that SHIO could serve as an artificial tapetum lucidum in a low-light environment.

2.3. Visual adaptation and accommodations

Visual adaptation refers to the ability of the visual perception system to adapt to changes in light intensity, thereby improving the efficiency and accuracy of image recognition. This capability can be further classified into two subtypes: photopic adaptation, which occurs under normal lighting conditions, and scotopic adaptation, which takes place in low-light or dark environments (Fig. 7a). The visual adaptation is achieved through a combination of subsequent processes, such as adjusting the intensity of incident light through the iris and

the adaptation through the optic nerves in the retina. Visual accommodation is another critical aspect of the visual system that is conducted by adjusting the focal length to obtain clear images of objects at different distances. In the eye of terrestrial animals, including humans, the shape of the lens changes with the support of the ciliary body acting as a contractile muscle, while in the eye of aquatic animals, such as fish and octopus, the position of the lens is adjusted by using retractor and protractor muscles to achieve visual accommodation (Fig. 7b).

Various operating mechanisms, including electromagnetic heating,[143] electrowetting in microfluidics,[144,145] and piezo-mechanisms[146] have been employed to fabricate adjustable aperture devices that mimic the adaptation function of the iris.
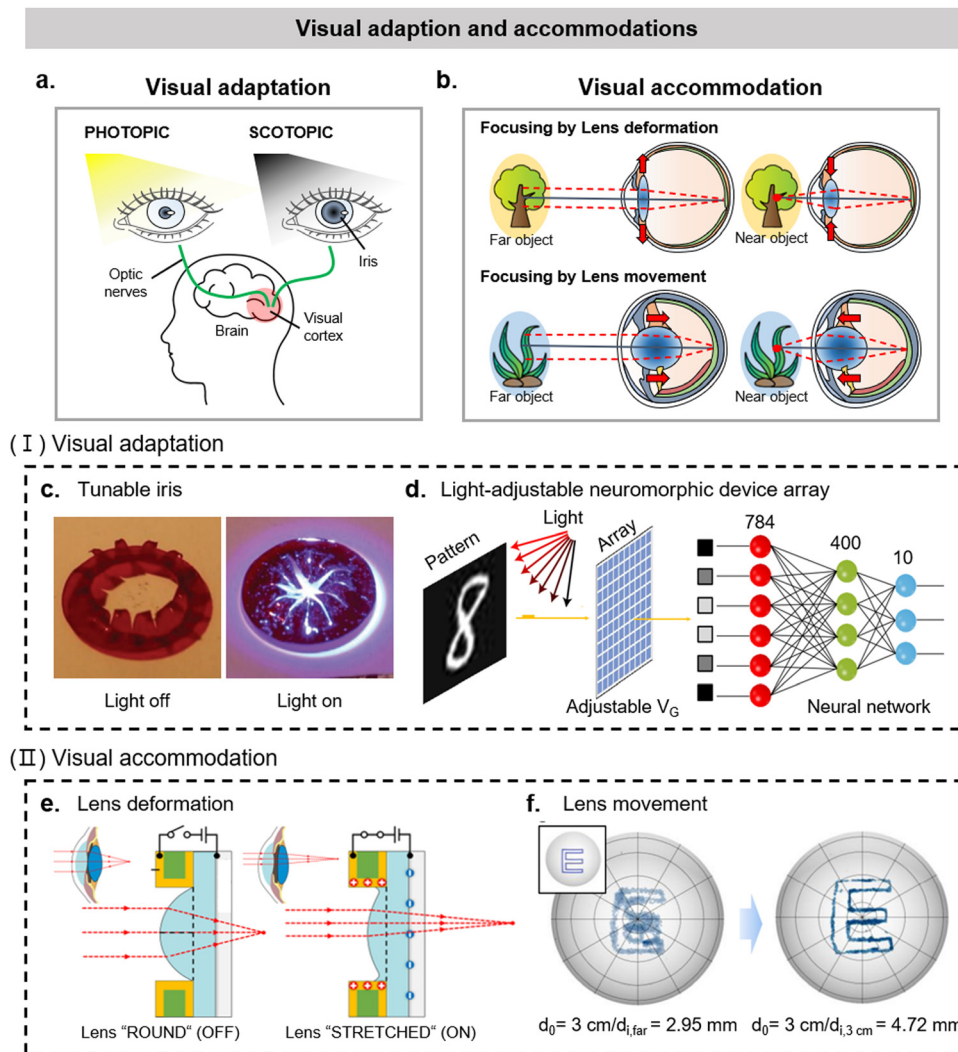
Fig. 7 Artificial vision systems that mimic visual adaptation and accommodation. (a) Schematic illustrations of the process of visual adaptation under different illumination. (b) Comparison of the visual accommodation by lens deformation and lens movement. (c) Photograph of self-regulating tunable iris when no light illumination (left) and light illumination (right) on it. Reproduced with permission.[147] Copyright 2017, Advanced Materials. (d) Schematic illustrations of vision sensor array for visual adaptation in a human eye. Reproduced with permission.[151] Copyright 2022, Nature Electronics. (e) Cross-sectional image of the bio-inspired PVC gel microlens system without (left) and with (right) the electrical simulation. Insets represent visual accommodation in a human eye. Reproduced with permission.[153] Copyright 2017, Scientific Reports. (f) Simple visual accommodation inspired by fish eye for a close object (object distance, d_o and image distance, d_i). Inset shows image of the original object. The image captured at $d_{i,far}$ = 2.95 mm is blurred (left) and refocused at $d_{i,3cm}$ = 4.72 mm (right). Reproduced with permission.[77] Copyright 2020, Nature Electronics.

However, these mechanisms require additional external systems for proper operation, which leads to the bulk device configuration. Zeng *et al.* implemented a self-regulating iris, which responds to the incident light intensity with no external control circuitry (Fig. 7c).[147] The actuation of the device is conducted through the anisotropic thermal expansion of light-responsive liquid crystal elastomers (LCEs) and radial molecular alignment of the iris segment. With an increase in the power of the incident light, there is an inward deformation of 12 individual segments, resulting in a reduction of the aperture's overall size. The device exhibits a light transmission of over 20 mW across input levels ranging from 30 mW to 200 mW. Meanwhile, the closure of the device occurs within 30 s under an incident light intensity of 230 mW cm^{-2}, and within 5 s at an irradiation level

of 300 mW cm^{-2}. When the eye is exposed to light that exceeds its dynamic range, the feedback through the optic nerve enables modulation of the incident optical signal into an appropriate level of electrical signal.

Several imaging devices have been developed to realize visual adaptation inspired by natural neural feedback systems.[148] Conventional systems usually depend on a voltage dividing strategy along with de-noising algorithms and post-processing techniques to extract useful information. However, these methods often result in decreased efficiency and increased complexity.[149,150] Liao *et al.* developed a vision sensor array that can emulate the human vision's scotopic and photopic adaptation function by utilizing the light intensity-dependent and time-dependent properties of MoS$_2$ (molybdenum disulfide)

phototransistors (Fig. 7d).[151] Introducing charge trap states on the surface of MoS$_2$ transistors allows the storage of light information and modulation of optoelectronic characteristics. When different gate voltages are applied, the channel conductivity can be dynamically adjusted, and the recognition range of the device can be expanded to be operated under varying light intensity conditions. The vision system consisting of an adaptive MoS$_2$ optical transistor array and a three-layer artificial neural network (ANN) was constructed to quantitatively evaluate the visual adaptation in terms of an image recognition rate. The recognition rate increased from 38.6% in 2s to 96.9% in 40 s for scotopic adaptation and increased from 9.5% in 2 s to 96.1% in 80 s for photopic adaptations, showing a clear improvement in both cases.

Liquid-state and solid-state materials have been widely used for lens systems to implement tunable focus. However, such systems have faced challenges, including fluidic leakages in liquid-state systems and the complicated mechanical control parts to modify the curvature of the lens in solid-state systems.[152] To implement the adjustable focal length without such issues, Bae *et al.* introduced a polyvinyl chloride (PVC) gel-based adaptive microlens system (Fig. 7e).[153] The reversible change in volume of the PVC gel with the electrical simulation results in a reduction of the sagittal height of the plano-convex PVC gel microlens, leading to changes in its focal length. The proposed system exhibited a significant change in focal length ($\sim$500%) under an electric field, and it showed a rapid response speed ($\leq$0.68 s), quiet actuation, and low power consumption (12 mW). Furthermore, inspired by the simple visual accommodation of aquatic animal eyes, Kim *et al.* presented an aquatic-vision-inspired camera that can adjust the focus *via* lens movement (Fig. 7f).[77] Objects located at a distance ranging from 20 cm to infinity have a nearly constant focal length of approximately 2.95 mm; however, as the object approaches the lens ($<$20 cm), the focal length gradually increases, and the image becomes blurred. The focused image can be achieved by simply adjusting the relative position of the photodetector array and the lens. In addition to adjusting the curvature or position of the lens, visual accommodation can be achieved by controlling the curvature of the photodetector array. Jung *et al.* demonstrated the dynamically tunable electronic eye that can change the radii of curvature of the photodetector array on the elastomeric membranes. The fabricated system also has a zoom ability, wide FoV, and low aberrations through tunable plano-convex lenses and hemispheric detector arrays.[154]

2.4. Other optical properties

The important features of natural vision, including high resolution, high sensitivity, visual adaptation, and accommodations, were introduced in the previous chapters. Also, the artificial devices that realize these features of natural vision have been reviewed so far. In this section, we will examine the specialized optical properties that biological organisms have evolved to adapt to their specific circumstances more effectively.

One of the unique optical characteristics of the cuttlefish eye is polarized vision.[155] Cuttlefish can detect their prey even when they are camouflaged in a complex background. This is because they possess photoreceptor cells with microvilli arranged in horizontal or vertical stacks. The arrangement helps the cuttlefish to extract polarized light reflected from the target object while filtering out random polarized background noise. This enhances the visual contrast and makes it easier for the cuttlefish to spot its prey. Kim *et al.* implemented such property by introducing flexible CNT-polymer composite film (Fig. 8a).[88] To fabricate the film, a mixture of single-wall carbon nanotubes (SWCNTs) and P(VDF-TrFE-CFE) was prepared and then subjected to a mild heat treatment while being mechanically stretched. This process obtained a film that was four times longer than its original length, and the SWCNTs were aligned within the composite material. The film served as artificial microvilli by absorbing polarized light parallel to the alignment, while transmitting light perpendicular to the alignment. Due to the flexibility of the film, it can be conformally laminated on the top surface of the curved photodiode array. When the photodiode was exposed to perpendicularly-polarized light under a light intensity of 16.0 mW cm^{-2}, a photocurrent of about 58 nA was measured. In contrast, no significant photocurrent was detected when the light was polarized parallel to the film. To evaluate the polarized imaging ability of the artificial vision system, target objects were created using polarized lights. A cross-shaped object was made with perpendicularly polarized light, and a diamond-shaped object was added around the cross-shaped object, which emitted polarized light parallel to the aligned CNTs. With the general vision, the cross-shaped object was obscured by the diamond-shaped object, but with polarization vision, the cross-shaped object was successfully detected.

Inspired by the tapetal structure found in the compound eye of morpho butterflies, Garcia *et al.* developed a multispectral imaging device (Fig. 8b).[156] Multiple layers of cytoplasm and air are stacked alternatively to form the natural tapetal structure, functioning as an interference filter.[157,158] The filter is located at the proximal end of the rhabdom in each ommatidium and selectively reflects light that is not absorbed by the visual and screening pigment. Then the reflected light gets an additional chance to be absorbed before leaving the eye. Each ommatidium has a different combination of visual pigments and stack structures, which have selective sensitivity to different wavelengths of light. Artificial tapetal filters were fabricated by stacking thin dielectric layers of SiO$_2$ and TiO$_2$ alternatively, and integrated with a CMOS image sensor array. The individual filters are designed to impart selective spectral sensitivity to the sensors, which can transmit particular light spectra while blocking others. The optimized transmittance of the filter is 60% and 80% for the visible and NIR light, respectively. Therefore, the device can simultaneously detect red, green, and blue (RGB) visible lights and near-infrared (NIR) light information in a real-time essential for surgical applications. The multispectral capability of the device was demonstrated by mapping a 4T1 breast cancer of murine and human sentinel lymph nodes (SLNs) during surgery.

Mantis shrimp (stomatopod) have evolved a highly advanced apposition compound eye.[159,160] The compound eye of the
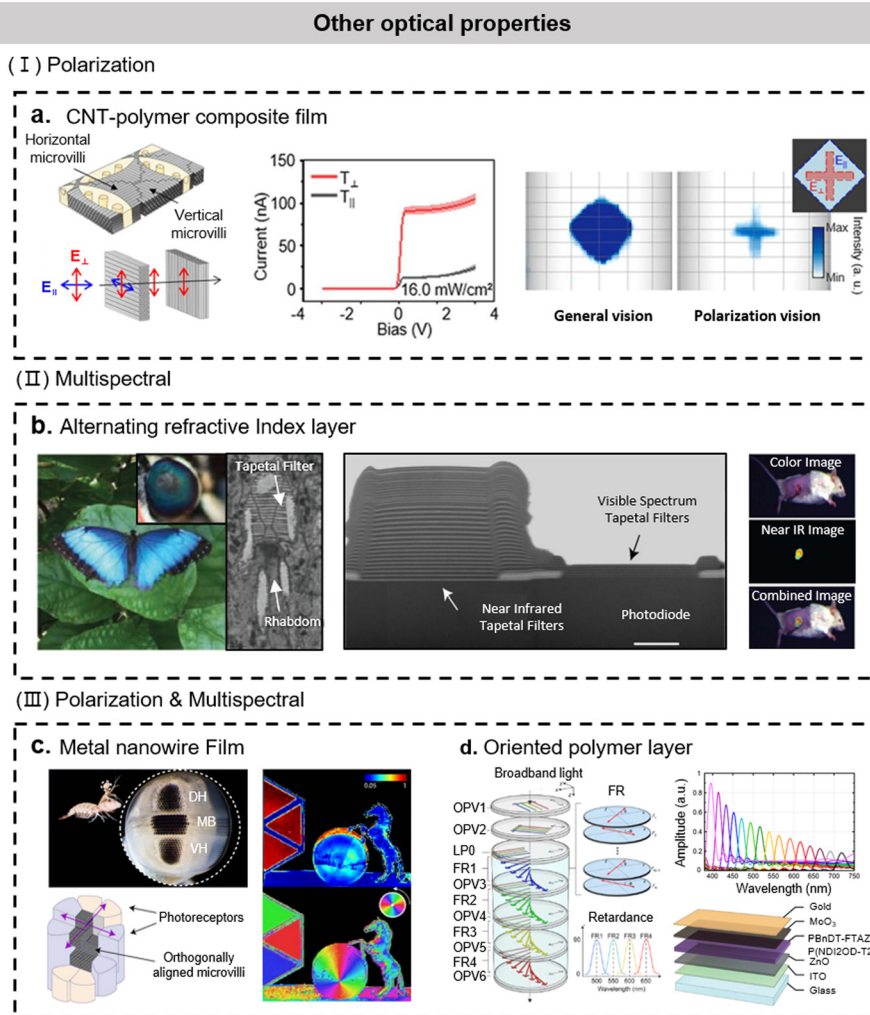
Fig. 8 Artificial vision systems that mimic special optical properties. (a) Schematic illustrations of orthogonally-arranged microvilli found in cuttlefish eye (left). $I-V$ curves of the cuttlefish-inspired image sensor under parallel-polarized ($T_{\parallel}$) and cross-polarized ($T_{\perp}$) illumination (middle). Imaging demonstration proves the polarization capability of the device (right). Reproduced with permission.[88] Copyright 2023, Science Robotics. (b) Photograph of the compound eye of morpho butterfly and cross-sectional TEM image of individual ommatidia (left). Cross-sectional TEM image of photodiode with artificial tapetal filters (middle). Single-exposure CMOS camera can only capture one of the two images: color image (right top) and near IR image (right middle), while the bio-inspired imager can capture both of them to produce combined image (right bottom). Reproduced with permission.[156] Copyright 2018, Optica. (c) Photograph of the compound eye structure of mantis shrimp (left top) and schematic illustration of ommatidia (left bottom). False-colormaps demonstrating polarization sensitive characteristics of the sensor (right). Reproduced with permission.[166] Copyright 2018, Optica. (d) Schematic diagram of the single-pixel image sensor structure (left). Absorption spectra for 15 stacked OPV-FR pairs (right top) and detailed structure of organic photovoltaic layer (right bottom). Reproduced with permission.[167] Copyright 2021, Science Advances.

mantis shrimp comprises thousands of ommatidia, containing spectrally selective or polarization sensing units. They are vertically stacked along a single optical axis that gives the mantis shrimp a wider range of color recognition[8] and the ability to detect the orientation of polarized lights.[161] The narrow mid-band (MB), ventral hemisphere (VH) and dorsal hemisphere (DH) are the three main parts of the eye.[162] The polarization vision of the mantis shrimp is based on the ommatidia in DH and VH regions that have orthogonally stacked interdigitating microvilli. The ommatidia in MB also contain photoreceptors that are sensitive to circular polarization.[163] The multispectral vision of the mantis shrimp is based on the rest of the MB, where 12 spectral-sensitive

photoreceptor cells with a sensing range from UV to far-red exist.[159,164,165]

Garcia *et al.* presented a CMOS photodetector array integrated with polarization filters inspired by the Mantis shrimp eye (Fig. 8c).[166] An individual photodetector comprises one p-type metal oxide semiconductor (PMOS), two n-type metal oxide semiconductor (NMOS), and a photodiode. The photodetector array shows logarithmic response due to the forward bias operation, unlike reverse bias operation in conventional photodetectors. The pixelated 2×2 polarization filters with an offset of $45°$ are repeated to cover the entire photodetector array. The aluminum nanowires in dimensions of 250 nm $\times$ 75 nm are used to fabricate the filters that mimic the arranged

microvilli of mantis shrimp. The integrated sensor array shows a high dynamic range of 140 dB and a signal-to-noise ratio (SNR) of 61 dB. Snapshot imaging is conducted to demonstrate the high-dynamic range and polarization capabilities of the sensor.

As an additional example of Mantis shrimp-inspired image sensing devices, Altaqui *et al.* proposed a single-pixel image sensor capable of performing hyperspectral and polarization sensing (Fig. 8d).[167] To compose the sensor, a linear polarizer (LP), six layers of panchromatic organic photovoltaic (OPV) detectors and four layers of folded polymer retarders (FRs) are stacked along a single optical axis, where the last four detectors alternate with FRs. This color-selective structure can detect 15 spectral bands of visible spectrum range from 400 to 750 nm. Based on PBnDT-FTAZ:P(NDI2OD-T2) bulk

heterojunction, the active polymer semiconductor layer is oriented by physically rubbing the layer in a certain direction, enabling high dichroic ratios that reduce optical crosstalk. Due to the polymers' orientation and anisotropic optical properties, the OPV cells can achieve polarization sensitivity. The experimental setup is constructed to verify the sensor's spectral and polarization imaging acquisition ability to detect four spectral channels with high spectral reconstruction accuracy.

Jumping spider (Salticidae) has developed precise depth perception ability to navigate complex environments and hunt their prey efficiently.[168] Although jumping sider has a relatively simple neural network system, they achieve this ability using specialized optics. They mainly use their principal eyes, which contain multilayered retinas.[169] Thus, multiple visual information with varying degrees of defocus can be received
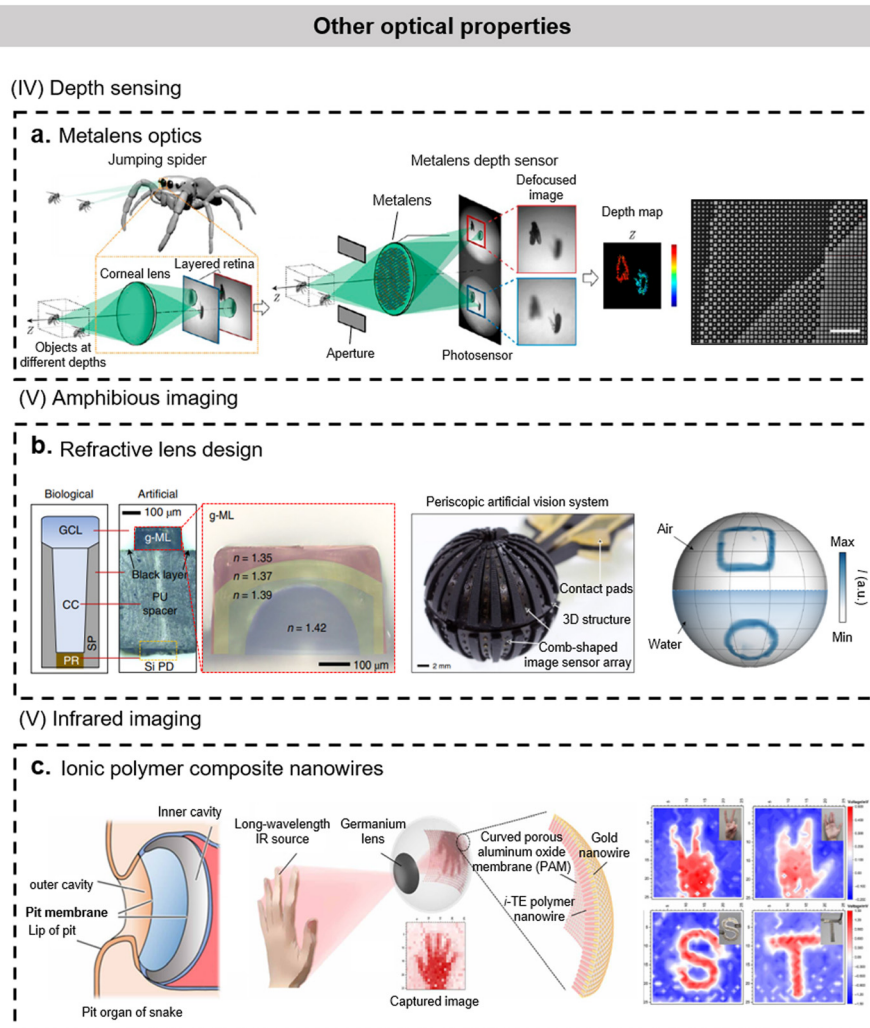

Fig. 9 Artificial vision systems that mimic special optical properties. (a) Depth sensing mechanism of the jumping spider (left). Metalens depth sensor inspired by the jumping spider (middle) and top-view SEM image of the metalens (right). Reproduced with permission.[171] Copyright 2019, PNAS. (b) Comparison between biological crab eye ommatidia and artificial image sensor with the detailed refractive profile of g-ML (left). Photograph of a crab-eye inspired periscopic artificial vision system (middle). Imaging demonstration proves amphibious imaging capability of the system (right). Reproduced with permission.[172] Copyright 2022, Nature Electronics. (c) Schematic illustration of the detailed pit organ structure of snake (left). Schematic of the working mechanism and structure of biomimetic IR image sensor (middle). Captured images of human hand gestures and letter-shaped resistors using the sensor (right). Reproduced with permission.[185] Copyright 2022, Science Advances.

simultaneously and used to determine the distance with relatively minimal computation.[170] Inspired by the depth sensing mechanism of the jumping spider, Guo *et al.* fabricated a depth sensor by exploiting metalens optics (Fig. 9a).[171] The building block of the metalens is composed of cuboid titanium dioxide (TiO_2) nanopillars on a glass substrate with a uniform height of 600 nm, varying width of 90–190 nm and center-to-center distance of 230 nm. This structure serves as a truncated waveguide and enables the local phase control from 0 to 2π, while maintaining a high transmission rate. Therefore, the phase profiles of two off-axis lenses, which have different in-focus distances on the aperture, can be incorporated. In this way, the incident light passing through the same aperture can simultaneously be separated to form two distinct defocused images on a single-plane photodetector. The depth information can be accurately measured by computing the point spread function of two different focal plane images. The sensor can capture fast-moving objects like fruit flies or water streams and translucent structures like flames, generating real-time depth and confidence maps.

Inspired by the compound eye of the fiddler crab (Uca arcuata) that lives in an intertidal habitat, Lee *et al.* developed an amphibious image sensor to maintain imaging capability both in the air and underwater (Fig. 9b).[172] While other crab species that lives in either terrestrial[14,173–176] or aquatic[177–179] environments have curved cornea surface and do not have amphibious imaging capability, the fiddler crab has a flat cornea surface with graded RI that prevents the loss of focus caused by changes in the external environment.[52] The ommatidia of fiddler crab consist of a graded-index corneal lens (GCL), crystalline cone (CC) and photoreceptor (PR).[52] The sensor pixel imitates this structure, integrating graded microlens (g-ML), polyurethane (PU) spacer and silicon photodiode vertically. The black sprayed layer coated around the g-ML resembles the screening pigment of the natural eye, which prevents optical crosstalk by blocking unwanted stray lights. The comb-shaped sensor array is then mounted on the 3D spherical mold to fabricate the imaging device. An imaging demonstration was conducted to verify the amphibious imaging capability of the device, and it showed stable imaging performance regardless of the external medium changes.

Unlike other visions that accept and perceive light through photoreceptors, some snake uses a quite different mechanism to detect IR light.[180] For example, pit vipers utilize their pit organs, which contain a temperature-sensitive transient receptor potential (TRP) channel, to detect and hunt small warm-blooded preys.[181–183] The pit organ does not directly recognize IR rays but detects subtly increasing temperatures in environments to obtain information about IR rays.[184] Inspired by this mechanism, Ding *et al.* presented a study on a self-powered hemispheric IR imaging device using the thermoelectric effect (Fig. 9c).[185] The device used a nanowire consisting of a polymer-based ionic thermoelectric material (i-TE) and gold in a porous aluminum oxide membrane. Compared to conventional IR sensing materials (*e.g.*, poly-silicon), the i-TE exhibits a superior Seebeck coefficient and low thermal conductivity.[186,187] Here,

the mobility of cations (Na^+) and anions ($TSFI^-$) varies depending on whether the material is p-type or n-type. When a temperature difference exists, charge separation occurs due to the difference in the degree to which thermal diffusion occurs, and IR imaging is possible through the resulting voltage. In addition, the curved hemispherical structure enables a wide FoV of $135°$ while reducing imaging aberrations and minimizing IR transmittance losses. The final device consists of 625 pixels and can be self-powered due to the thermoelectric effect. It possesses high responsivity of 0.5 mV for a 40 °C object that have 5 cm distance from the device. The IR-imaging demonstration showed that the device could successfully distinguish imaging targets like human hand gestures and letter-shaped resistors.

3. Summary and remaining challenges

Visual functions of the biological eyes, especially highly efficient image acquisition capabilities developed through the natural evolutionary process, were reviewed. These features include high resolution, high sensitivity, visual adaption, and visual accommodation functions. Accordingly, to overcome the limitations of the conventional imaging system, the state-of-the-art artificial imaging devices inspired by the optically-superior and structurally-compact natural vision systems were reviewed. Recent advances in novel materials, device designs, and fabrication strategies that facilitated the realization of these biomimetic devices were also reviewed. More detailed summary for each section is as follows.

First, high-resolution vision systems were reviewed. Bio-inspired lens structures that can correct optical aberrations and prevent optical crosstalk have been introduced. Facile design strategies, including aspherical surfaces, gradient refractive indices, minimized optical crosstalk *via* light-absorbers, and optical waveguides enable the development of highly resolvable artificial lenses. Apart from the optical structure, the curved morphology of the device was also examined, utilizing the optimized design of the device structure and metal interconnections. Intrinsically flexible 2D materials such as graphene and MoS_2 can be employed to introduce additional functionalities to devices and facilitate the attainment of curved morphologies. Moreover, the utilization of spatially variable density of photodetectors, with a high-density photodetector array distributed in the main visual region, can contribute to the efficient realization of high resolution.

Next, the review covered high-sensitivity artificial vision systems specifically designed for low-intensity light imaging and night-time vision. These systems incorporate an adjustable aperture that reduces the F-number, allowing them to capture more light. The superposition-type compound eye inspires multiple layered structures on the photodetectors, which can amplify the incoming light signal. In addition, the antireflective nanostructure of the moth eye provides a way to reduce the light loss by the surface reflection and increase the light transmission. To enhance light absorption and sensitivity at

the retinal level, various techniques were employed, including surface modification, the use of light-accumulating structures (such as glass microcups with reflective sidewalls), and the incorporation of a rear light reflector (such as an inverse opal hydrogel).

Thirdly, the visual adaptation and accommodation functions, which are two critical features of the natural eye to perceive objects in different lighting conditions and at different distances, were reviewed. The light-actuated liquid crystal elastomer can change its shape in response to different light levels, and light-adjustable neuromorphic devices have been developed to mimic adaptive capabilities. Some creatures have evolved to adapt to more special situations *via* unique optical functions such as polarization recognition, multispectral imaging, depth sensing, amphibious imaging, and IR vision. Polarization and multispectral imaging were imitated by applying various functional films (*e.g.*, CNT-polymer composite, SiO_2–TiO_2 alternating layer, metal nanowire film, oriented polymer layer). Depth sensing was realized through metalens optics. Flat surface lens with a graded refractive index enables amphibious imaging that can reserve focal length regardless to external medium changes. IR sensing based on the thermoelectric effect was also achieved by using ionic polymer composite nanowires.

Although recent advances in bio-inspired artificial vision systems resolve various issues in conventional imaging devices, there are remaining challenges; low pixel density (*i.e.*, low resolution), limited functions, and lack of real-time response. These challenges mainly come from limitation of the fabrication equipment in university laboratories. In the case of low pixel density, the fabrication scale of small-sized pixels is limited to hundreds of micrometers, while commercial CMOS image sensors achieve a few-micrometer pixel scale (Table 1). Even in bio-inspired vision systems that have achieved a high pixel density using flat CMOS sensors, the full potential of the high pixel density is not utilized due to the mismatch between the lens and the flat image plane. Especially for the compound eye system, the lens size of the artificial ommatidium is much larger compared to the pixel size. As a result, the resolution of the image sensor system significantly decreases, which becomes vulnerable to noisy inputs. To overcome the limitation, the mechanical system to ameliorate the low resolution is introduced, but it often degrades the system frame rate, which hinders the real-time imaging demonstration.

Another challenge is to integrate the multiple functions observed in natural eyes into a single device capable of adapting to dynamic and complex situations. Most previous works have focused on reproducing a specific function of natural eyes, such as high-resolution or high-sensitivity. However, in real-world situations, imaging devices need to perform multiple functions simultaneously and adapt themselves immediately to the changes of external circumstances. As most of the artificial vision studies rely on manual operation, it is necessary to integrate various system components that perform different roles, such as power supply, motors, computing devices, and control devices. The entire system might become bulky, making it challenging to be integrated with mobile electronics and

robotics. Besides, the entire device system should endure harsh environmental changes (*e.g.*, humidity, extreme temperatures, dust) and maintain their performance for a reasonable time. Hence, further research is required to fully harness the advantages of biomimetic imaging devices.

Nonetheless, notable advancements and progress are continuously being developed in this field, establishing the potential to revolutionize advanced imaging devices in the future. The advancements have begun with the researchers who have focused on giving curvature to rigid materials to fabricate curved image sensors. Optimized designs of the device structure and novel fabrication techniques with mechanical analysis have been conducted to mitigate the trade-offs between high resolution and high curvature of the image sensor array. Then, research has expanded to encompass the entire biological vision system, which includes lenses, apertures, and nanophotonic structures. In addition to the studies focused on the effective image acquisition ability *via* unique optical structures, there have been advancements in image data processing techniques that imitate biological nerve systems. These techniques involve electronic synapses and neuromorphic sensors capable of in-sensor computing, enabling efficient processing of massive image data. Integrating these image acquisition and image data processing capabilities can be a first step towards developing a complete biomimetic imaging system. If the aforementioned issues are successfully addressed and the optimal device is designed by considering the relevant parameters in each situation, the artificial vision systems currently in the research stage are expected to contribute further for real-life applications.

Conflicts of interest

The authors declare no conflicts of interest.

Acknowledgements

References

1 M. O'Connor, D.-E. Nilsson and A. Garm, *J. Comp. Physiol., A*, 2010, **196**, 213–220.

2 I. R. Schwab, *Eye*, 2018, **32**, 302–313.

3 M. Wilson, *J. Comp. Physiol.*, 1978, **124**, 297–316.

4 M. Friedrich, *Arthropod Struct. Dev.*, 2006, **35**, 357–378.

5 M. F. Land and R. D. Fernald, *Annu. Rev. Neurosci.*, 1992, **15**, 1–29.

6 F. Pichaud, A. Briscoe and C. Desplan, *Curr. Opin. Neurobiol.*, 1999, **9**, 622–627.

7 S. Yokoyama, *Gene*, 2002, **300**, 69–78.

8 T. W. Cronin and N. J. Marshall, *Nature*, 1989, **339**, 137–140.

9 D. Osorio and M. Vorobyev, *Proc. R. Soc. B*, 2005, **272**, 1745–1752.

10 D. E. Nilsson and S. Pelger, *Proc. R. Soc. B*, 1994, **256**, 53–58.

11 M. F. Land, *Annu. Rev. Entomol.*, 1997, **42**, 147–177.

12 E. Warrant and M. Dacke, *Annu. Rev. Entomol.*, 2011, **56**, 239–254.

13 K. Kirschfeld, Neural principles in vision, 1976.

14 D. E. Nilsson, *Nature*, 1988, **332**, 76–78.

15 S. R. Detwiler, *Yale J. Biol. Med.*, 1938, **10**, 485.

16 L. Harkness and H. C. Bennet-Clark, *Nature*, 1978, **272**, 814–816.

17 A. Bringmann, *Anat., Histol., Embryol.*, 2019, **48**, 177–200.

18 R. J. Pumphrey, *J. Exp. Biol.*, 1948, **25**, 299–312.

19 O. Lind, M. Mitkus, P. Olsson and A. Kelber, *Proc. R. Soc. B*, 2014, **281**, 20132209.

20 J. Cilulko, P. Janiszewski, M. Bogdaszewski and E. Szczygielska, *Eur. J. Wildl. Res.*, 2013, **59**, 17–23.

21 J. K. Bowmaker, *Nature*, 1980, **284**, 306.

22 E. A. Newman and P. H. Hartline, *Sci. Am.*, 1982, **246**, 116–127.

23 M. S. Kim, M. S. Kim, G. J. Lee, S.-H. Sunwoo, S. Chang, Y. M. Song and D.-H. Kim, *Adv. Mater. Technol.*, 2022, **7**, 2100144.

24 C. Choi, H. Seung and D.-H. Kim, *IEEE Journal on Flexible Electronics*, 2022, **1**, 76–87.

25 Z. Long, X. Qiu, C. L. J. Chan, Z. Sun, Z. Yuan, S. Poddar, Y. Zhang, Y. Ding, L. Gu, Y. Zhou, W. Tang, A. K. Srivastava, C. Yu, X. Zou, G. Shen and Z. Fan, *Nat. Commun.*, 2023, **14**, 1972.

26 M. F. Land and D.-E. Nilsson, *Animal Eyes*, Oxford University Press, 2012.

27 L. P. Lee and R. Szema, *Science*, 2005, **310**, 1148–1150.

28 Laikin, Milton, Crc Press, 2018.

29 J.-U. Lee and S.-M. Yu, *J. Opt. Soc. Korea*, 2009, **13**, 184–192.

30 T. Chung, Y. Lee, S. Yang, K. Kim, B. Kang and K. Jeong, *Adv. Funct. Mater.*, 2018, **28**, 1705912.

31 G. J. Lee, C. Choi, D. Kim and Y. M. Song, *Adv. Funct. Mater.*, 2018, **28**, 1705202.

32 T. Wu, S. S. Hamann, A. C. Ceballos, C. E. Chang, O. Solgaard and R. T. Howe, *Microsyst. Nanoeng.*, 2016, **2**, 1–9.

33 K. H. Jeong, J. Kim and L. P. Lee, *Science*, 2006, **312**, 557–561.

34 D. A. Atchison, *Optics of the human eye*, CRC Press, 2023.

35 C. Choi, M. K. Choi, S. Liu, M. Kim, O. K. Park, C. Im, J. Kim, X. Qin, G. J. Lee, K. W. Cho, M. Kim, E. Joh, J. Lee, D. Son, S.-H. Kwon, N. L. Jeon, Y. M. Song, N. Lu and D.-H. Kim, *Nat. Commun.*, 2017, **8**, 1664.

36 D. E. Nilsson, *Philos. Trans. R. Soc. Lond., B, Biol. Sci.*, 2009, **364**, 2833–2847.

37 D. E. Nilsson and D. Arendt, *Curr. Biol.*, 2008, **18**, R1096–R1098.

38 E. M. Caves, N. C. Brandley and S. Johnsen, *Trends. Ecol. Evol.*, 2018, **33**, 358–372.

39 E. J. Warrant, T. W. Cronin, S. Johnsen and N. J. Marshall, Visual ecology, Princeton University Press, 2014.

40 W. M. Harmening, P. Nikolay, J. Orlowski and H. Wagner, *J. Visualization*, 2009, **9**, 13.

41 L. Reymond, *Vision Res.*, 1985, **25**, 1477–1491.

42 J. Eklöf, *Vision in echolocating bats*, 2003.

43 K. W. Spence, *J. Comp. Psychol.*, 1934, **18**, 333.

44 C. Tappeiner, S. Gerber, V. Enzmann, J. Balmer, A. Jazwinska and M. Tschopp, *Front. Zool.*, 2012, **9**, 10.

45 M. Williamson and A. Keast, *Can. J. Zool.*, 1988, **66**, 2840–2846.

46 B. K. P. PhD and R. C. A. PhD, *Clin. Exp. Optom.*, 1993, **76**, 22–25.

47 A. Chaudhuri, P. E. Hallett and J. A. Parker, *Vision Res.*, 1983, **23**, 1351–1363.

48 R. H. H. Kroger, M. C. W. Campbell, R. D. Fernald and H. J. Wagner, *J. Comp. Physiol., A*, 1999, **184**, 361–369.

49 B. K. Pierscionek and J. W. Regini, *Prog. Retinal Eye Res.*, 2012, **31**, 332–349.

50 J. Cai, J. P. Townsend, T. C. Dodson, P. A. Heiney and A. M. Sweeney, *Science*, 2017, **357**, 564–569.

51 Y. L. Gagnon, D. Wilby and S. E. Temple, *J. Opt. Soc. Am. A*, 2016, **33**, 1901–1909.

52 A. Alkaladi and J. Zeil, *J. Comp. Neurol.*, 2014, **522**, 1264–1283.

53 R. Levi-Setti, *Trilobites*, University of Chicago Press, 1995.

54 E. J. Warrant and P. D. McIntyre, *Prog. Neurobiol.*, 1993, **40**, 413–461.

55 K. Franze, J. Grosche, S. N. Skatchkov, S. Schinkinger, C. Foja, D. Schild, O. Uckermann, K. Travis, A. Reichenbach and J. Guck, *Proc. Natl. Acad. Sci. U. S. A.*, 2007, **104**, 8287–8292.

56 A. Reichenbach and A. Bringmann, *Glia*, 2020, **68**, 768–796.

57 J. Park, H. Seung, D. C. Kim, M. S. Kim and D. H. Kim, *Adv. Funct. Mater.*, 2021, **31**, 2009281.

58 C. Choi, J. Leem, M. S. Kim, A. Taqieddin, C. Cho, K. W. Cho, G. J. Lee, H. Seung, H. J. Bae, Y. M. Song, T. Hyeon, N. R. Aluru, S. W. Nam and D. H. Kim, *Nat. Commun.*, 2020, **11**, 5934.

59 W. Gao, Z. Xu, X. Han and C. Pan, *Nano Today*, 2022, **42**, 101366.

60 J. J. Kim, H. Liu, A. Ousati Ashtiani and H. Jiang, *Rep. Prog. Phys.*, 2020, **83**, 047101.

61 G. Zuccarello, D. Scribner, R. Sands and L. J. Buckley, *Adv. Mater.*, 2002, **14**, 1261–1264.

62 M. F. Land, *Contemp. Phys.*, 1988, **29**, 435–455.

63 A. Smitha and P. Jidesh, *J. Mod. Opt.*, 2021, **68**, 1002–1017.

64 Y. M. Song, H. G. Park, G. J. Lee and J. S. Park, Smart Sensors and Systems: Innovations for Medical, Environmental, and IoT Applications, 2017, 157–174.

65 F. Crescitelli, *Photochemistry of vision*, 1972, **7**, 245–363.

66 R. Navarro, *J. Optom.*, 2009, **2**, 59.

67 B. O'Brien, *J. Opt. Soc. Am.*, 1951, **41**, 882–894.

68 N. Watanuki, G. Kawamura, S. Kaneuchi and T. Iwashita, *Fish. Sci.*, 2000, **63**, 417–423.

69 C. M. Talbot and J. N. Marshall, *Philos. Trans. R. Soc. Lond., B, Biol. Sci.*, 2011, **366**, 724–733.

70 Z. Zhan, K. Wang, H. Yao and Z. Cao, *Appl. Opt.*, 2009, **48**, 4375–4380.

71 C. V. Brown, G. G. Wells, M. I. Newton and G. McHale, *Nat. Photonics*, 2009, **3**, 403–405.

72 C.-W. Chen and F.-G. Tseng, The 13th International Conference on Solid-State Sensors, Actuators and Microsystems, Digest of Technical Papers. TRANSDUCERS'05., IEEE, 2005, 376–379.

73 K. Mishra, C. Murade, B. Carreel, I. Roghair, J. M. Oh, G. Manukyan, D. Van Den Ende and F. Mugele, *Sci. Rep.*, 2014, **4**, 6378.

74 S. Ji, M. Ponting, R. S. Lepkowicz, A. Rosenberg, R. Flynn, G. Beadie and E. Baer, *Opt. Express*, 2012, **20**, 26746–26754.

75 S. Ji, K. Yin, M. Mackey, A. Brister, M. Ponting and E. Baer, *Opt. Eng.*, 2013, **52**, 112105.

76 R. Dylla-Spears, T. D. Yee, K. Sasan, D. T. Nguyen, N. A. Dudukovic, J. M. Ortega, M. A. Johnson, O. D. Herrera, F. J. Ryerson and L. L. Wong, *Sci. Adv.*, 2020, **6**, eabc7429.

77 M. S. Kim, G. J. Lee, C. Choi, M. S. Kim, M. Lee, S. Liu, K. W. Cho, H. M. Kim, H. Cho, M. K. Choi, N. Lu, Y. M. Song and D. H. Kim, *Nat. Electron.*, 2020, **3**, 546–553.

78 S. Wu, T. Jiang, G. Zhang, B. Schoenemann, F. Neri, M. Zhu, C. Bu, J. Han and K. D. Kuhnert, *Artif. Intell. Rev.*, 2017, **48**, 573–603.

79 J. Vannier, B. Schoenemann, T. Gillot, S. Charbonnier and E. Clarkson, *Nat. Commun.*, 2016, **7**, 10320.

80 K. Kim, K. W. Jang, J. K. Ryu and K. H. Jeong, *Light: Sci. Appl.*, 2020, **9**, 28.

81 B. Dai, L. Zhang, C. Zhao, H. Bachman, R. Becker, J. Mai, Z. Jiao, W. Li, L. Zheng, X. Wan, T. J. Huang, S. Zhuang and D. Zhang, *Nat. Commun.*, 2021, **12**, 6458.

82 H. C. Ko, M. P. Stoykovich, J. Song, V. Malyarchuk, W. M. Choi, C. J. Yu, J. B. Geddes, J. Xiao, S. Wang, Y. Huang and J. A. Rogers, *Nature*, 2008, **454**, 748–753.

83 B. Guenter, N. Joshi, R. Stoakley, A. Keefe, K. Geary, R. Freeman, J. Hundley, P. Patterson, D. Hammon and G. Herrera, *Opt. Express*, 2017, **25**, 13010–13023.

84 K. Itonaga, T. Arimura, K. Matsumoto, G. Kondo, K. Terahata, S. Makimoto, M. Baba, Y. Honda, S. Bori and T. Kai, 2014 Symposium on VLSI Technology (VLSI-Technology): Digest of Technical Papers, IEEE, 2014, pp. 1–2.

85 Y. M. Song, Y. Xie, V. Malyarchuk, J. Xiao, I. Jung, K. J. Choi, Z. Liu, H. Park, C. Lu, R. H. Kim, R. Li, K. B. Crozier, Y. Huang and J. A. Rogers, *Nature*, 2013, **497**, 95–99.

86 D. Floreano, R. Pericet-Camara, S. Viollet, F. Ruffier, A. Brückner, R. Leitel, W. Buss, M. Menouni, F. Expert, R. Juston, M. K. Dobrzynski, G. L'Eplattenier, F. Recktenwald, H. A. Mallot and N. Franceschini, *Proc. Natl. Acad. Sci. U. S. A.*, 2013, **110**, 9267–9272.

87 K. Zhang, Y. H. Jung, S. Mikael, J. H. Seo, M. Kim, H. Mi, H. Zhou, Z. Xia, W. Zhou, S. Gong and Z. Ma, *Nat. Commun.*, 2017, **8**, 1782.

88 M. Kim, S. Chang, M. Kim, J. E. Yeo, M. S. Kim, G. J. Lee, D. H. Kim and Y. M. Song, *Sci. Robot.*, 2023, **8**, eade4698.

89 D. B. Phillips, M. J. Sun, J. M. Taylor, M. P. Edgar, S. M. Barnett, G. M. Gibson and M. J. Padgett, *Sci. Adv.*, 2017, **3**, e1601782.

90 M. F. Land, *Handbook of sensory physiology*, 1981, **6**, 471–592.

91 E. Warrant, *The senses: a comprehensive reference*, Elsevier, 2007, pp. 53–86.

92 L. M. Mäthger, R. T. Hanlon, J. Håkansson and D. E. Nilsson, *Vision Res.*, 2013, **83**, 19–24.

93 C. J. Murphy and H. C. Howland, *J. Exp. Zool.*, 1990, **256**, 22–28.

94 D. H. Ko, J. R. Tumbleston, K. J. Henderson, L. E. Euliss, J. M. Desimone, R. Lopez and E. T. Samulski, *Soft Matter*, 2011, **7**, 6404–6407.

95 A. R. Parker and H. E. Townley, *Nat. Nanotechnol.*, 2007, **2**, 347–353.

96 D. G. Stavenga, S. Foletti, G. Palasantzas and K. Arikawa, *Proc. R. Soc. B*, 2006, **273**, 661–667.

97 L. P. Lee and R. Szema, *Science*, 2005, **310**, 1148–1150.

98 E. J. Warrant, *Vision Res.*, 1999, **39**, 1611–1630.

99 H. Savin, P. Repo, G. Von Gastrow, P. Ortega, E. Calle, M. Garín and R. Alcubilla, *Nat. Nanotechnol.*, 2015, **10**, 624–628.

100 H. J. Wagner, E. Fröhlich, K. Negishi and S. P. Collin, *Prog. Retinal Eye Res.*, 1998, **17**, 637–685.

101 M. Kreysing, R. Pusch, D. Haverkate, M. Landsberger, J. Engelmann, J. Ruiter, C. Mora-Ferrer, E. Ulbricht, J. Grosche, K. Franze, S. Streif, S. Schumacher, F. Makarov, J. Kacza, J. Guck, H. Wolburg, J. K. Bowmaker, G. Von Der Emde, S. Schuster, H. J. Wagner, A. Reichenbach and M. Francke, *Science*, 2012, **336**, 1700–1703.

102 H. J. Arnott, N. J. Maciolek and J. A. C. Nicol, *Science*, 1970, **169**, 478–480.

103 L. Zueva, A. Zayas-Santiago, L. Rojas, P. Sanabria, J. Alves, V. Tsytsarev and M. Inyushin, *J. Biophotonics*, 2022, **15**, e202200002.

104 S. Vee, G. Barclay and N. H. Lents, *BioEssays*, 2022, **44**, 2200003.

105 F. J. Ollivier, D. A. Samuelson, D. E. Brooks, P. A. Lewis, M. E. Kallberg and A. M. Komáromy, *Vet. Ophthalmol.*, 2004, **7**, 11–22.

106 N. A. Locket, *Proc. R. Soc. London, Ser. B*, 1974, **186**, 281–290.

107 R. Gunter, H. G. W. Harding and W. S. Stiles, *Nature*, 1951, **168**, 293–294.

108 S. G. Kim, D. Kim, S. Kim, J. Yoon and H. S. Lee, *Macromol. Mater. Eng.*, 2019, **304**, 1800560.

109 D.-E. Nilsson, *Bioscience*, 1989, **39**, 298–307.

110 D. Keum, K.-W. Jang, D. S. Jeon, C. S. H. Hwang, E. K. Buschbeck, M. H. Kim and K.-H. Jeong, *Light: Sci. Appl.*, 2018, **7**, 80.

111 H. M. Kim, M. S. Kim, G. J. Lee, Y. J. Yoo and Y. M. Song, *Opt. Express*, 2019, **27**, 4435–4444.

112 H. M. Kim, M. S. Kim, G. J. Lee, H. J. Jang and Y. M. Song, *Sensors*, 2020, **20**, 2129.

113 H. M. Kim, Y. J. Yoo, J. M. Lee and Y. M. Song, *Sensors*, 2022, **22**, 3455.

114 H. M. Kim, M. S. Kim, S. Chang, J. Jeong, H. G. Jeon and Y. M. Song, *Micromachines*, 2021, **12**, 1453.

115 Q. Fan, W. Xu, X. Hu, W. Zhu, T. Yue, C. Zhang, F. Yan, L. Chen, H. J. Lezec, Y. Lu, A. Agrawal and T. Xu, *Nat. Commun.*, 2022, **13**, 2130.

116 V. Van Duong, T. N. Huu, J. Yim and B. Jeon, *IEEE Trans. Comput. Imaging*, 2023, **9**, 350–366.

117 X. Hua, Y. Wang, S. Wang, X. Zou, Y. Zhou, L. Li, Y. Feng, C. Xun, X. Shumin, T. Din Ping, H. Jiecai, W. Zhenlin and S. Zhu, *Nat. Commun.*, 2022, **13**, 2732.

118 H. G. Jeon, J. Park, G. Choe, J. Park, Y. Bok, Y. W. Tai and I. So Kweon, Proceedings of the IEEE conference on computer vision and pattern recognition, 2015, 1547–1555.

119 Y. Bok, H. G. Jeon and I. S. Kweon, IEEE transactions on pattern analysis and machine intelligence, 2016, 39, 287–300.

120 C. C. Huang, X. Wu, H. Liu, B. Aldalali, J. A. Rogers and H. Jiang, *Small*, 2014, **10**, 3050–3057.

121 Y. Kanamori, M. Sasaki and K. Hane, *Opt. Lett.*, 1999, **24**, 1422–1424.

122 C. G. Choi, Y. T. Han, J. T. Kim and H. Schift, *Appl. Phys. Lett.*, 2007, **90**, 221109.

123 A. Kaless, U. Schulz, P. Munzert and N. Kaiser, *Surf. Coat. Technol.*, 2005, **200**, 58–61.

124 B. J. Bae, S. H. Hong, E. J. Hong, H. Lee and G. Y. Jung, *Jpn. J. Appl. Phys.*, 2009, **48**, 010207.

125 Q. Chen, G. Hubbard, P. A. Shields, C. Liu, D. W. E. Allsopp, W. N. Wang and S. Abbott, *Appl. Phys. Lett.*, 2009, **94**, 263118.

126 S. S. Oh, C. G. Choi and Y. S. Kim, *Microelectron. Eng.*, 2010, **87**, 2328–2331.

127 V. Garg, R. G. Mote and J. Fu, *Opt. Mater.*, 2019, **94**, 75–85.

128 Y. M. Song, E. S. Choi, G. C. Park, C. Y. Park, S. J. Jang and Y. T. Lee, *Appl. Phys. Lett.*, 2010, **97**, 093110.

129 Y. T. Lee, Y. M. Song, S. J. Jang and J. S. Yu, *Small*, 2010, **6**, 984–987.

130 J. Sun, X. Wang, J. Wu, C. Jiang, J. Shen, M. A. Cooper, X. Zheng, Y. Liu, Z. Yang and D. Wu, *Sci. Rep.*, 2018, **8**, 5438.

131 Y. J. Yoo, Y. J. Kim, S.-Y. Kim, J. H. Lee, K. Kim, J. H. Ko, J. W. Lee, B. H. Lee and Y. M. Song, *Opt. Mater. Express*, 2019, **9**, 4178–4186.

132 C. Il Yeo, Y. Min Song, S. Jun Jang and Y. Tak Lee, *J. Appl. Phys.*, 2013, **114**, 024305.

133 Y. J. Yoo, K. S. Chang, S. W. Hong and Y. M. Song, *Opt. Quantum Electron.*, 2015, **47**, 1503–1508.

134 M. Kim, S. Jang, J. Choi, S. M. Kang and M. Choi, *Nano-Micro Lett.*, 2019, **11**, 1–10.

135 W. I. Nam, Y. J. Yoo and Y. M. Song, *Opt. Express*, 2016, **24**, A1033–A1044.

136 K. H. Tsui, Q. Lin, H. Chou, Q. Zhang, H. Fu, P. Qi and Z. Fan, *Adv. Mater.*, 2014, **26**, 2805–2811.

137 J. Y. Chen and K. W. Sun, *Sol. Energy Mater. Sol. Cells*, 2010, **94**, 629–633.

138 C. Il Yeo, J. B. Kim, Y. M. Song and Y. T. Lee, *Nanoscale Res. Lett.*, 2013, **8**, 1–7.

139 Y. Gao, H. Cansizoglu, K. G. Polat, S. Ghandiparsi, A. Kaya, H. H. Mamtaz, A. S. Mayet, Y. Wang, X. Zhang, T. Yamada, E. P. Devine, A. F. Elrefaie, S. Y. Wang and M. S. Islam, *Nat. Photonics*, 2017, **11**, 301–308.

140 N. V. Hoang, A. Pereira, H. S. Nguyen, E. Drouard, B. Moine, T. Deschamps, R. Orobtchouk, A. Pillonnet and C. Seassal, *ACS Photonics*, 2017, **4**, 1705–1712.

141 H. Liu, Y. Huang and H. Jiang, *Proc. Natl. Acad. Sci. U. S. A.*, 2016, **113**, 3982–3985.

142 K. Min, S. Kim and S. Kim, *Proc. Natl. Acad. Sci. U. S. A.*, 2017, **114**, 6185–6190.

143 S. Schuhladen, F. Preller, R. Rix, S. Petsch, R. Zentel and H. Zappe, *Adv. Mater.*, 2014, **26**, 7247–7251.

144 P. Muller, R. Feuerstein and H. Zappe, *J. Microelectromech. Syst.*, 2012, **21**, 1156–1164.

145 S. Schuhladen, K. Banerjee, M. Stürmer, P. Müller, U. Wallrabe and H. Zappe, *Light: Sci. Appl.*, 2016, **5**, e16005–e16005.

146 J. Draheim, T. Burger, J. G. Korvink and U. Wallrabe, *Opt. Lett.*, 2011, **36**, 2032–2034.

147 H. Zeng, O. M. Wani, P. Wasylczyk, R. Kaczmarek and A. Priimagi, *Adv. Mater.*, 2017, **29**, 1701814.

148 J.-K. Song, J. Kim, J. Yoon, J. H. Koo, H. Jung, K. Kang, S.-H. Sunwoo, S. Yoo, H. Chang, J. Jo, W. Baek, S. Lee, M. Lee, H. J. Kim, M. Shin, Y. J. Yoo, Y. M. Song, T. Hyeon, D.-H. Kim and D. Son, *Nat. Nanotechnol.*, 2022, **17**, 849–856.

149 S. M. Kwon, S. W. Cho, M. Kim, J. S. Heo, Y. H. Kim and S. K. Park, *Adv. Mater.*, 2019, **31**, 1906433.

150 O. Liba, K. Murthy, Y. T. Tsai, T. Brooks, T. Xue, N. Karnad, Q. He, J. T. Barron, D. Sharlet, R. Geiss, S. W. Hasinoff, Y. Pritch and M. Levoy, *ACM Trans. Graph.*, 2019, **38**, 164.

151 F. Liao, Z. Zhou, B. J. Kim, J. Chen, J. Wang, T. Wan, Y. Zhou, A. T. Hoang, C. Wang, J. Kang, J. H. Ahn and Y. Chai, *Nat. Electron.*, 2022, **5**, 84–91.

152 S. Petsch, S. Schuhladen, L. Dreesen and H. Zappe, *Light: Sci. Appl.*, 2016, **5**, e16068–e16068.

153 J. W. Bae, E. J. Shin, J. Jeong, D. S. Choi, J. E. Lee, B. U. Nam, L. Lin and S. Y. Kim, *Sci. Rep.*, 2017, **7**, 2068.

154 I. Jung, J. Xiao, V. Malyarchuk, C. Lu, M. Li, Z. Liu, J. Yoon, Y. Huang and J. A. Rogers, *Proc. Natl. Acad. Sci. U. S. A.*, 2011, **108**, 1788–1793.

155 N. Shashar, C. Milbury and R. Hanlon, *Mar. Freshwater Behav. Physiol.*, 2002, **35**, 57–68.

156 M. Garcia, C. Edmiston, T. York, R. Marinov, S. Mondal, N. Zhu, G. P. Sudlow, W. J. Akers, J. Margenthaler, S. Achilefu, R. Liang, M. A. Zayed, M. Y. Pepino and V. Gruev, *Optica*, 2018, **5**, 413–422.

157 W. H. Miller and G. D. Bernard, *J. Ultrastruct. Res.*, 1968, **24**, 286–294.

158 D. G. Stavenga, *Nature*, 1975, **254**, 435–437.

159 H. H. Thoen, M. J. How, T. H. Chiou and J. Marshall, *Science*, 2014, **343**, 411–413.

160 J. Marshall and J. Oberwinkler, *Nature*, 1999, **401**, 873–874.

161 I. M. Daly, M. J. How, J. C. Partridge, S. E. Temple, N. J. Marshall, T. W. Cronin and N. W. Roberts, *Nat. Commun.*, 2016, **7**, 12140.

162 J. Marshall, T. W. Cronin and S. Kleinlogel, *Arthropod Struct. Dev.*, 2007, **36**, 420–448.

163 N. W. Roberts, T.-H. Chiou, N. J. Marshall and T. W. Cronin, *Nat. Photonics*, 2009, **3**, 641–644.

164 N. J. Marshall, *Nature*, 1988, **333**, 557–560.

165 M. J. Bok, N. W. Roberts and T. W. Cronin, *Proc. R. Soc. B*, 2018, **285**, 20181384.

166 M. Garcia, T. Davis, S. Blair, N. Cui and V. Gruev, *Optica*, 2018, **5**, 1240–1246.

167 A. Altaqui, P. Sen, H. Schrickx, J. Rech, J. W. Lee, M. Escuti, W. You, B. J. Kim, R. Kolbas, B. T. O'Connor and M. Kudenov, *Sci. Adv.*, 2021, **7**, eabe3196.

168 G. Menda, P. S. Shamble, E. I. Nitzany, J. R. Golden and R. R. Hoy, *Curr. Biol.*, 2014, **24**, 2580–2585.

169 M. F. Land, *J. Exp. Biol.*, 1958, **51**, 443–470.

170 T. Nagata, M. Koyanagi, H. Tsukamoto, S. Saeki, K. Isono, Y. Shichida, F. Tokunaga, M. Kinoshita, K. Arikawa and A. Terakita, *Science*, 2012, **335**, 469471.

171 Q. Guo, Z. Shi, Y. W. Huang, E. Alexander, C. W. Qiu, F. Capasso and T. Zickler, *Proc. Natl. Acad. Sci. U. S. A.*, 2019, **116**, 22959–22965.

172 M. Lee, G. J. Lee, H. J. Jang, E. Joh, H. Cho, M. S. Kim, H. M. Kim, K. M. Kang, J. H. Lee, M. Kim, H. Jang, J. E. Yeo, F. Durand, N. Lu, D. H. Kim and Y. M. Song, *Nat. Electron.*, 2022, **5**, 452–459.

173 P. Castro, P. Davie, D. Guinot, F. Schram and C. von Vaupel Klein, Treatise on Zoology-Anatomy, Taxonomy, Biology. The Crustacea, Volume 9 Part C (2 Vols): Brachyura, Brill, 2015.

174 P. K. L. Ng, C. D. Schubart and C. Lukhaup, *Raffles Bull. Zool.*, 2015, **63**, 3–13.

175 P. T. Green, *Crustaceana*, 2004, **77**, 125–128.

176 K. Arikawa, K. Kawamata, T. Suzuki and E. Eguchi, *J. Comp. Physiol., A*, 1987, **161**, 161–174.

177 C. L. McLay, Brachyura and crab-like Anomura of New Zealand, University of Auckland Marine Laboratory, 1988.

178 E. Eguchi, M. Dezawa and V. B. Meyer-Rochow, *Biol. Bull.*, 1997, **192**, 300–308.

179 J. Luque, W. T. Allison, H. Bracken-Grissom, K. Jenkins, A. R. Palmer, M. Porter and J. Wolfe, *BioRxiv*, 2019, 786087.

180 H. A. Schraft, G. S. Bakken and R. W. Clark, *Sci. Rep.*, 2019, **9**, 3950.

181 P. H. Hartline, L. Kass and M. S. Loop, *Science*, 1978, **199**, 1225–1229.

182 E. A. Newman and P. H. Hartline, *Science*, 1981, **213**, 789–791.

183 E. O. Gracheva, N. T. Ingolia, Y. M. Kelly, J. F. Cordero-Morales, G. Hollopeter, A. T. Chesler, E. E. Sánchez, J. C. Perez, J. S. Weissman and D. Julius, *Nature*, 2010, **464**, 1006–1011.

184 G. S. Bakken and A. R. Krochmal, *J. Exp. Biol.*, 2007, **210**, 2801–2810.

185 Y. Ding, G. Liu, Z. Long, Y. Zhou, X. Qiu, B. Ren, Q. Zhang, C. Chi, Z. Wan, B. Huang and Z. Fan, *Sci. Adv.*, 2022, **8**, eabq8432.

186 D. Zhao, A. Würger and X. Crispin, *J. Energy Chem.*, 2021, **61**, 88–103.

187 C. G. Han, X. Qian, Q. Li, B. Deng, Y. Zhu, Z. Han, W. Zhang, W. Wang, S. P. Feng, G. Chen and W. Liu, *Science*, 2020, **368**, 1091–1098.

188 L. Gu, S. Poddar, Y. Lin, Z. Long, D. Zhang, Q. Zhang, S. Lei, Q. Xiao, K. Matthew, J. Ali and Z. Fan, *Nature*, 2022, **581**, 278–282.